

VoIgt profile Parameter Estimation Routine (VIPER): H I photoionization rate at $z < 0.5$

Prakash Gaikwad^{1*}, Raghunathan Srianand², Tirthankar Roy Choudhury¹, and Vikram Khaire¹

¹National Centre for Radio Astrophysics, Tata Institute of Fundamental Research, Pune 411007, India

²Inter-University Centre for Astronomy and Astrophysics (IUCAA), Post Bag 4, Pune 411007, India

ABSTRACT

We have developed a parallel code called “VoIgt profile Parameter Estimation Routine (VIPER)” for automatically fitting the H I Ly- α forest seen in the spectra of QSOs. We obtained the H I column density distribution function (CDDF) and line width (b) parameter distribution for $z < 0.45$ using spectra of 82 QSOs obtained using Cosmic Origins Spectrograph and VIPER. Consistency of these with the existing measurements in the literature validate our code. By comparing this CDDF with those obtained from hydrodynamical simulation, we constrain the H I photoionization rate (Γ_{HI}) at $z < 0.45$ in four redshift bins. The VIPER, together with the Code for Ionization and Temperature Evolution (CITE) we have developed for GADGET-2, allows us to explore parameter space and perform χ^2 minimization to obtain Γ_{HI} . We notice that the b parameters from the simulations are smaller than what are derived from the observations. We show the observed b parameter distribution and b vs $\log N_{\text{HI}}$ scatter can be reproduced in simulation by introducing sub-grid scale turbulence. However, it has very little influence on the derived Γ_{HI} . The $\Gamma_{\text{HI}}(z)$ obtained here, $(3.9 \pm 0.1) \times 10^{-14} (1+z)^{4.98 \pm 0.11} \text{ s}^{-1}$, is in good agreement with those derived by us using flux based statistics in the previous paper. These are consistent with the hydrogen ionizing ultra-violet (UV) background being dominated mainly by QSOs without needing any contribution from the non-standard sources of the UV photons.

Key words: cosmological parameters - cosmology: observations-intergalactic medium-QSOs: absorption lines-ultraviolet: galaxies

1 INTRODUCTION

The Ly- α forest absorption seen in the spectra of the luminous distant QSOs is one of the most sensitive tools to study the physical conditions of the intergalactic medium (IGM). In hierarchical structure formation models, Ly- α forest is thought to arise from the fluctuations in the cosmic density field (Bi et al. 1992; Bi 1993; Bi & Davidsen 1997; Croft et al. 1997, 1998). The strength and width of the Ly- α absorption lines can be used to trace the ionization and thermal state of the neutral hydrogen (H I) in the IGM. Thus observations of the Ly- α forest have regularly been used to constrain cosmological and astrophysical parameters related to IGM physics.

Various statistics are used in the literature to constrain cosmological and astrophysical parameters from the Ly- α forest observations. These statistics are broadly divided into two cases. In the first case, Ly- α transmitted flux is treated

as a continuous field quantity. In particular, the mean flux, the flux probability distribution function (PDF) and the flux power spectrum (PS) have been used to constrain cosmological parameters such as Ω_m , $\Omega_b h^2$, σ_8 and n_s (McDonald et al. 2000; Phillips et al. 2001; Choudhury et al. 2001; Tegmark et al. 2004; Viel et al. 2004a,b; McDonald et al. 2005; Seljak et al. 2006; Viel & Haehnelt 2006; Viel et al. 2006, 2009), thermal history parameters¹ (Zaldarriaga et al. 2001; Bolton et al. 2008; Lidz et al. 2010; Becker et al. 2011; Calura et al. 2012; Garzilli et al. 2015) and H I photoionization rate (Γ_{HI} ; Rauch et al. 1997; Meiksin & White 2004; Bolton & Haehnelt 2007; McQuinn et al. 2011; Becker & Bolton 2013; Pontzen et al. 2014; Gaikwad et al. 2017). Constraining such quantities by comparing flux statistics between observations and simulations are relatively easier and are frequently used in the high- z ($2 \leq z \leq 6$) studies.

¹ The thermal state of the IGM is described by the effective equation of state parameterized by the mean IGM temperature (T_0) and the slope (γ).

* E-mail: prakashg@ncra.tifr.res.in

In the second case, Ly- α forest is decomposed into multiple Voigt profiles. The line width distribution function calculated from Voigt profile fitting is sensitive to the thermal history and the energy injected by various astrophysical processes in the form of heat and turbulent motions in the IGM (Schaye et al. 1999, 2000; McDonald et al. 2001; Davé & Tripp 2001). Similarly, the column density distribution function (CDDF) calculated from Voigt profile decomposition is sensitive to Γ_{HI} (Cooke et al. 1997; Kollmeier et al. 2014; Shull et al. 2015; Gurvich et al. 2016) and cosmological parameters (Storrie-Lombardi et al. 1996; Penton et al. 2000; Shull et al. 2012). While statistics based on parameters obtained using Voigt profile fitting are useful in deriving thermal history and equation of state of the IGM, the Voigt profile decomposition is usually a time consuming process. Therefore, a large parameter space exploration in simulations is usually difficult.

To constrain Γ_{HI} using CDDF at low- z (i.e., $z < 0.5$), the UV spectrograph on space telescope is needed for the Ly- α forest observations. Thanks to Cosmic Origins Spectrograph onboard Hubble Space Telescope (hereafter HST-COS) we have good quality observations of the low- z Ly- α forest. These observations are used to place good constraints on Γ_{HI} (Kollmeier et al. 2014; Shull et al. 2015; Gaikwad et al. 2017). Previous measurement of Γ_{HI} using CDDF by Kollmeier et al. (2014, hereafter K14) and Shull et al. (2015, hereafter S15) are conflicting. S15 found a factor 3 smaller Γ_{HI} than K14². Note that both used the same HST-COS data but different cosmological simulations. Recently Gaikwad et al. (2017) (hereafter Paper-I) used same HST-COS data but different statistics namely flux PDF and flux PS to constrain Γ_{HI} with appropriate errorbars³. In contrast to K14 and S15, Paper-I varied Γ_{HI} as a free parameter, minimize the χ^2 for the two statistics and calculated appropriate statistical and systematic uncertainties in Γ_{HI} using covariance matrices for a range of IGM thermal histories. The Γ_{HI} measurements and its evolution obtained in Paper-I is found to be consistent with those from S15.

In this paper we measure the Γ_{HI} and associated errors at low- z using CDDF by varying Γ_{HI} as a free parameter. The basic idea behind constraining Γ_{HI} is to calculate the χ^2 between the observed CDDF, $f_{\text{obs}}(N_{\text{HI}}, z)$, and the CDDF, $\bar{f}_{\text{sim}}(N_{\text{HI}}, z, \Gamma_{\text{HI}})$, calculated by modeling the Ly- α forest in a cosmological simulation. The Γ_{HI} corresponding to minimum value of χ^2 (i.e. χ_{min}^2) gives the best fit Γ_{HI} whereas the associated statistical error is obtained by calculating the parameter values corresponding to $\chi_{\text{min}}^2 \pm 1$ (Press et al. 1992). The modeling of the Ly- α forest is relatively simple (Cen et al. 1994; Zhang et al. 1995; Miralda-Escudé et al. 1996; Hernquist et al. 1996) and well understood as they probe mildly non-linear densities of the IGM ($\Delta \sim 10$ at $z < 0.5$, see Table 2 in Paper-I). However, at low- z Ly- α absorption could originate from the extended circumgalactic medium of

star forming galaxies. The free parameter Γ_{HI} could be degenerate with thermal history parameters such as mean IGM temperature T_0 and slope of equation of state γ (as shown at $z \geq 2$ by Bolton et al. 2005; Bolton & Haehnelt 2007; Faucher-Giguère et al. 2008). In Paper-I, we developed a module named ‘‘Code for Ionization and Temperature Evolution (CITE)’’ that allows one to probe the wide range of thermal history and Γ_{HI} easily. Using CITE, we varied the thermal history parameters at high- z ($z = 2.1$) and evolved the IGM temperature up to $z = 0$. As shown in Paper-I, the thermal history parameters at low- z are found to be very similar $T_0 \sim 5000$ K and $\gamma \sim 1.6$ even if the initial parameters T_0 and γ at $z = 2.1$ are quite different. This implies that the Γ_{HI} derived at low- z are not very sensitive to the thermal history of the IGM at $z \sim 2$.

In order to obtain the CDDF, each Ly- α absorption is usually decomposed into multiple Voigt profile components. Each Voigt profile is defined by 3 free parameters i.e., line center (λ_c), H I column density (N_{HI}) and line width parameter (b). The manual Voigt decomposition of the large number (~ 10000) of simulated Ly- α forest is laborious and time consuming. Furthermore, the criteria used to fit the number of components (N_{Voigt}) to a given identified Ly- α absorption is subjective and need not be unique. Although there are several Voigt profile fitting codes available in the literature like VPFIT⁴, ALIS (Cooke et al. 2014), GVPFIT (Bainbridge & Webb 2016) it will be invaluable to have a tailor made automatic module that will identify Ly- α absorption regions and fit them with multiple component Voigt profiles where the best fit parameters of the individual components and the minimum number of required components are determined through objective criterion.

We have developed a parallel processing module ‘‘Voigt profile Parameter Estimation Routine’’ (VIPER) to fit the Ly- α forest with multiple Voigt profiles automatically. In VIPER, the blended and saturated features are fitted simultaneously with multi-component Voigt profiles. An objective criteria based on information theory is used to find the number of Voigt profiles needed to describe the Ly- α forest. The parallel and automated nature of VIPER allows us to simultaneously fit large number of simulated spectra and to explore a wide parameter space efficiently. For consistency, we used the same code for analyzing the observed and simulated spectra. We calculated CDDF by consistently taking into account the redshift path length and the incompleteness of the observed sample. We show CDDF and line width distribution obtained for observed data using VIPER matches very well with those from Danforth et al. (2016).

The paper is organized as follows. In §2 and §4 we explain the HST-COS data and cosmological simulation used in this work. §3 describes our module VIPER that automatically fits Voigt profiles to the Ly- α forest. In §5 we match observed CDDF with model CDDF to constrain Γ_{HI} in 4 different redshift bins defined in Paper-I. Finally we summarize our results in §6. Throughout this work we use flat Λ CDM cosmology with parameters ($\Omega_{\Lambda}, \Omega_{\text{m}}, \Omega_{\text{b}}, h, n_{\text{s}}, \sigma_8, Y$) \equiv (0.69, 0.31, 0.0486, 0.674, 0.96, 0.83, 0.24) reported by Planck Collaboration et al. (2015). All the distances are expressed in comoving co-ordinates unless and otherwise mentioned.

² The errorbars on Γ_{HI} are not evaluated systematically in either K14 or S15.

³ S15 analysis is based on ENZO which uses adaptive mesh refinement (AMR) technique. K14 used smoothed particle hydrodynamic GADGET-3 code. Whereas, Paper-I used smoothed particle hydrodynamic GADGET-2 code coupled with Code for Ionization and Temperature Evolution (CITE) see §4 for more detail. This allowed us to explore the parameter space in detail.

⁴ <http://www.ast.cam.ac.uk/~rfc/vpfit.html>

The H I photoionization rate Γ_{HI} in units of 10^{-12} s^{-1} is denoted by Γ_{12} .

2 HST-COS QSO ABSORPTION SPECTRA

We used publicly available HST-COS science data product⁵ that consists of a sample of low redshift Ly- α forest spectra towards 82 UV bright QSOs performed by Danforth et al. (2016, hereafter D16). These QSOs are distributed in the redshift range $z = 0.0628$ to 0.852 . The sample covers the Ly- α forest in the redshift range $0 \leq z \leq 0.48$ with a velocity resolution of $\sim 17 \text{ km s}^{-1}$ (full width at half maximum). The median signal-to-noise ratio (SNR) per pixel varies from 6 to 17 for different sightlines.

D16 fitted the continuum to each spectrum and identified several thousand absorption line features that consists of Ly- α lines, higher order Ly-series lines, metal lines from the IGM and the interstellar medium (ISM) of our Galaxy. As a part of the HST-COS science data product, D16 fitted each absorption feature with multiple component Voigt profiles and provided a table that contains line identifications (type of the specie and rest wavelength of the transition), redshift of the absorption system, column density, doppler- b parameter, equivalent width (along with associated fitting errors) and significance level of the absorption line detection. In this work we refer to their Ly- α line catalog as “D16 line catalog”.

As in Paper-I, we divided the sample into 4 different redshift bins (we denote them by roman numerals I, II, III and IV respectively) $\bar{z} \pm \Delta z \equiv (0.1125 \pm 0.0375, 0.2 \pm 0.05, 0.3 \pm 0.05, 0.4 \pm 0.05)$. The size and center of the lowest redshift bin is chosen in a way that avoids the contamination by geo-coronal line emission at $z \leq 0.075$. There are total 50, 31, 16 and 12 lines of sight in the redshift bins I, II, III and IV respectively. Apart from the intervening Ly- α lines all other lines in the Ly- α forest are treated as contamination in our spectra. We replace all other lines except Ly- α lines by the continuum added with a Gaussian random noise (see Fig. 2 in Paper-I). We use these clean spectra for further analysis.

3 AUTOMATIC VOIGT PROFILE FITTING CODE

In this section we describe our automated Voigt profile fitting procedure “Voigt profile Parameter Estimation Routine” (VIPER). The same code has been used to fit the observed and simulated Ly- α forest spectra to constrain Γ_{12} in §5 from CDDF. The algorithm is broadly divided into 3 steps; first we identify the absorption lines and region bracketing these lines, next in these regions we fit as many Voigt components as necessary based on an objective criteria. In the final step we accept the Voigt profile fit for a line based on a significance level of the fit. We now discuss each step in detail below.

⁵ <https://archive.stsci.edu/prepds/igm/>

(i) **Line and region identification** : Following Schneider et al. (1993) and D16, first we estimate the “crude significance level” (hereafter CSL) to identify the lines,

$$\text{CSL} = \frac{W(\lambda)}{\bar{\sigma}(\lambda)} \quad (1)$$

where $W(\lambda)$ and $\bar{\sigma}(\lambda)$ are “equivalent width vector” and “line-less error vector” respectively. The CSL defined in this way has the advantage that the unresolved features are unlikely to be identified as lines (see Schneider et al. 1993, for details). $W(\lambda)$ and $\bar{\sigma}(\lambda)$ are obtained by convolving the normalized flux and line-less error (i.e., error on flux if absorption lines were absent), respectively, with a representative line profile (see §2.3 of D16). The representative line profile is a convolution of Gaussian (of a Doppler parameter of $b = 20 \text{ km s}^{-1}$) with HST-COS line spread function (LSF). We repeated the procedure with different values of the doppler $b = 50, 100 \text{ km s}^{-1}$ to incorporate any missing narrower, broader and blended lines. The second panel from the top in Fig. 1 shows the CSL estimated for the spectrum shown in the top panel. Initially we identified all the lines with maxima satisfying $\text{CSL} \geq 1.5$ shown by red stars in second panel of Fig. 1⁶. Next we find a threshold on either side of the maxima to enclose the line in a region. A minimum is accepted as a threshold if $\text{CSL} < 1.5$. A minimum with $\text{CSL} > 1.5$ indicates that the lines are blended hence we search for the next minimum until we meet the condition $\text{CSL} < 1.5$ to accept it as a threshold. We then merge the overlapping regions (if any) into one bigger region for blended lines (e.g., see the yellow shaded region in second panel of Fig. 1). This procedure allows us to identify and fit the blended lines simultaneously.

(ii) **Voigt profile fitting** : In this step we fit each identified region by multiple Voigt profiles. Voigt profile, convolution of Gaussian with Lorentzian, is a real part of the “Faddeeva function” $w(z)$ (Armstrong 1967),

$$\begin{aligned} w(z) &= e^{-z^2} \text{erfc}(-iz) \\ w(x + iy) &= V(x, y) + iL(x, y) \end{aligned} \quad (2)$$

where $\text{erfc}(-iz)$ is the error function, $V(x, y)$ is Voigt profile and $L(x, y)$ is imaginary part of Faddeeva function. We used *wofz*⁷ function in *python’s scipy* package to compute Voigt profile. We convolve this Voigt profile with the appropriate HST-COS LSF before performing χ^2 minimization⁸. For χ^2 minimization, we used *leastsq*⁹ function in *python’s scipy* package. If $F_{\text{obs}}, \sigma_{\text{obs}}, F_{\text{fit}}(\lambda_c, b, N_{\text{HI}})$ are observed flux, error in the observed flux and fitted Ly- α flux respectively then

⁶ The cutoff used in this work is smaller than that used by D16 ($\text{CSL} \geq 3$). This results in more number of identified lines in our initial line catalog as compared to D16. However, in the final step most of the extra identified lines at lower significance level are rejected.

⁷ http://ab-initio.mit.edu/wiki/index.php/Faddeeva_Package

⁸ We assumed that the observed fluxes in different pixels are uncorrelated. HST-COS LSF is not a Gaussian (http://www.stsci.edu/hst/cos/performance/spectral_resolution/). This function is slightly asymmetric around the center and has extended wings.

⁹ <https://docs.scipy.org/doc/scipy-0.18.1/reference/generated/scipy.optimize.leastsq.html>

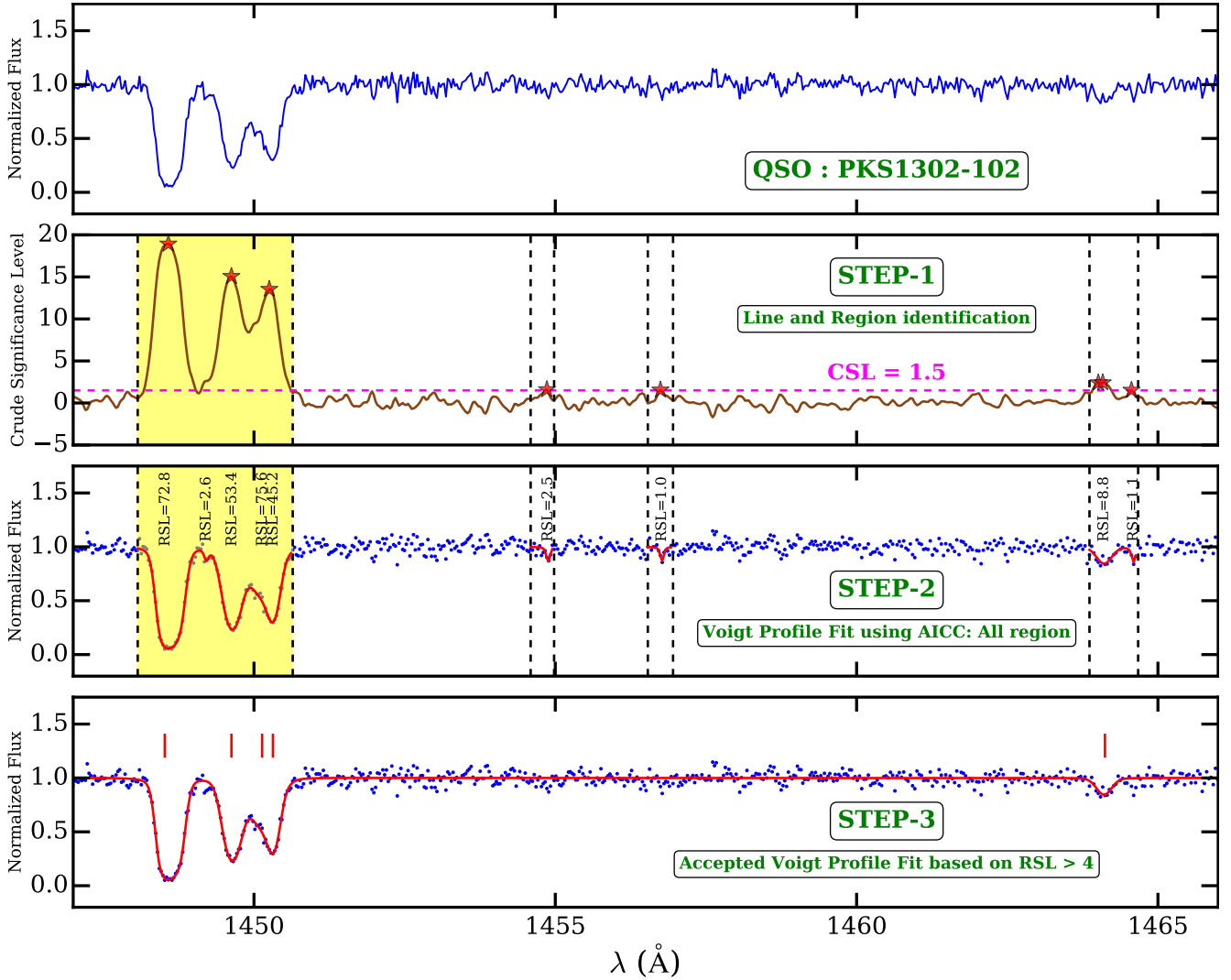


Figure 1. Illustration of different steps in the automatic Voigt profile fitting procedure used in VIPER. *Top* panel shows a portion of the observed HST-COS spectrum along the sightline towards QSO PKS1302-102. *Second* panel from top shows the estimation of crude significance level (CSL) using the Eq.1 (for $b = 20 \text{ km s}^{-1}$). All the identified peaks with $\text{CSL} \geq 1.5$ (magenta dashed line) are shown by red stars. The identified regions enclosing the peaks are shown by black dashed vertical lines. Overlapping regions are merged accordingly to fit blended lines simultaneously (see yellow shaded region). All the identified regions are fitted with Voigt profile as shown in the third panel from top. The number of components used to fit the region is decided using AICC and demanding $\chi^2_{\text{dof}} \sim 1$ (see §3). Rigorous significance level (RSL) for each fitted line is calculated using Eq.4. *Bottom* panel shows the accepted fit with the $\text{RSL} \geq 4$.

we minimize the function $(F_{\text{obs}} - F_{\text{fit}})/\sigma_{\text{obs}}^2$ in *leastsq* routine. The fit parameters are allowed to vary over the range $5 \leq b \text{ (km s}^{-1}\text{)} \leq 150$, $10 \leq \log(N_{\text{HI}}/\text{cm}^{-2}) \leq 16.5$ and λ_c bounds are set by the wavelength of the region. We set initial guess values for lines in a given region by fitting individual line in that region with a Gaussian. Note that in the previous step each identified line is enclosed in two CSL minima hence we can fit each line separately. However initial guess values for any additional line required by the information criteria (explained below) are set randomly in the region.

A criteria based on information theory, Akaike Information Criteria with Correction (AICC) (Akaike 1974; Liddle 2007; King et al. 2011) is used to assess the optimum number of Voigt profile components required for an acceptable fit. If p is the number of parameters in a model used to fit

the data with n pixels, then the AICC is given by,

$$\text{AICC} = \chi^2 + \frac{2pn}{(n-p-1)} \quad (3)$$

The first term on right-hand side is a measure of loss of information while describing the data with a model. The second term in right-hand side quantifies the complexity of the model. Thus AICC incorporates the trade-off between loss of information and complexity of the model. We assign a model to be the best fit model over the previously assigned best fit model if AICC is lower by at least 5 (Jeffreys 1961). Since only the relative difference in the AICC values is important, according to Jeffreys (1961) $\Delta\text{AICC} = 5$ is considered as the strong evidence against the weaker model. Fig. 2 illustrates our method of choosing a best fit model. Black points in left-hand panel of the Fig. 2 are data points which we want to fit by Voigt profile model. We fitted the data with

different number of (say $N_{\text{Voigt}} = 1, 2, 3, 4, 5$) Voigt profiles. The resulting AICC and χ^2 for each model as a function of N_{Voigt} is shown by star and circle respectively in the right-hand panel of the Fig. 2. For $N_{\text{Voigt}} = 1$ the model is less complex but the χ^2 ($\chi_{\text{dof}}^2 \sim 1.5$) between model and data is large (see green curve in left-hand panel) resulting in a larger AICC value¹⁰. Whereas, for $N_{\text{Voigt}} > 2$, the χ^2 ($\chi_{\text{dof}}^2 \sim 1.0$) is small (see blue curve in left-hand panel) but with increasing N_{Voigt} the complexity of the model increases and hence AICC also increases. It is interesting to note that the χ^2 remains nearly constant for $N_{\text{Voigt}} \geq 2$ whereas AICC systematically increases for $N_{\text{Voigt}} > 2$. A model simply based on χ^2 minimization, thus would be degenerate for $N_{\text{Voigt}} \geq 2$. The minimum AICC occurs for $N_{\text{Voigt}} = 2$ (black arrow showing red star in right-hand panel) which shows trade-off between goodness-of-fit ($\chi_{\text{dof}}^2 \sim 0.9$) and complexity of the model. The corresponding best fit model is shown by red curve in left-hand panel. Thus for minimum AICC, χ_{dof}^2 is also close to 1 and hence we chose it to be the best fit model. In the third panel from top of Fig. 1, we show the results of fitting each region with as many Voigt components as necessary for the minimum AICC and $\chi_{\text{dof}}^2 \sim 1$.

(iii) **Significance level of fitted lines** : Initially we fitted the lines that are identified using a simple approximation of ‘‘Crude Significance Level’’. However, we used a ‘‘Rigorous Significance Level’’ (hereafter RSL) formula (Keeney et al. 2012) to include the lines in the final line catalog as given below,

$$\text{RSL} = (\text{SNR})_1 \frac{W_\lambda}{\Delta\lambda} \frac{\eta(x)}{x} f_c(x, \lambda, b) \quad (4)$$

where, x is width (in pixels) of discrete region over which equivalent width W_λ is calculated, $\Delta\lambda = \lambda/x$, λ is width (in Å) of the discrete region, $f_c(x, \lambda, b)$ is the fractional area of the HST-COS LSF contained within the region of integration, $\eta(x) = (\text{SNR})_x / (\text{SNR})_1$ takes care of the fact that noise property may not be purely Poissonian, $(\text{SNR})_1$ is signal to noise ratio per pixel, $(\text{SNR})_x$ signal to noise ratio average over discrete region containing x pixels. We used the parametric form of $\eta(x)$, $f_c(x, \lambda, b)$ given by Keeney et al. (2012), their Eq. 4, Eq. 7 to Eq. 11 with parameters given in Table.1 for the coadded data).

To avoid the spurious detection, we retain only feature measured with $\text{RSL} > 4$ in the final line catalog. Other features are excluded from further analysis. Using this criteria, we find that the number of identified lines with $\log N_{\text{HI}} \geq 12.4$ to be fitted by VIPER (1277 H I Ly- α lines) are similar to those of D16 (1280 H I Ly- α lines)¹¹. In the third panel from top of Fig. 1, we show the RSL for each fitted component above the line. Bottom panel of Fig. 1 shows that

¹⁰ The reduced χ^2 is given by,

$$\chi_{\text{dof}}^2 = \frac{\chi^2}{n - p}$$

where $n = 134$ is number of pixels in the given region (left-hand panel of Fig. 2), $p = 3 \times N_{\text{Voigt}}$ is number of free parameters where factor 3 accounts for the number of free parameters in each Voigt component (λ_c , N_{HI} and b).

¹¹ The total number of identified lines above completeness limit (i.e., $\log N_{\text{HI}} \geq 13.6$) in VIPER and D16 line catalog is 533 and 522 respectively.

the final accepted Voigt profile fit that contains only those components which have $\text{RSL} > 4$.

The comparison of Voigt profile fit of VIPER with that of D16 method is illustrated in Fig. 3. The fit from VIPER and D16 method is shown by solid red and dashed blue line respectively. The line centers of components fitted by VIPER and D16 method are shown by solid red and dashed blue vertical ticks respectively. For VIPER the reduced χ^2 is small as compared to that for the components obtained by D16. The top row shows the example where VIPER fit (in terms of number of component and the values of fitted parameter along with the errorbar) matches well with D16 fit. In most situations the fitted parameters from VIPER matched well with those from D16 within errors. In few cases VIPER fitted data better than D16 method (bottom row of Fig. 3) in terms of reduced χ^2 . We fitted all the observed spectra using VIPER and form a line catalog ‘‘VIPER catalog’’ (see Appendix for details). It should be noted that unlike D16, VIPER does not fit higher order Lyman series lines (e.g. Ly- β , Ly- γ) simultaneously for an accurate measurement of $\log N_{\text{HI}}$ in the case of saturated Ly- α lines. However, we show in the next section that the differences in CDDF and line width distributions from ‘‘VIPER catalog’’ and ‘‘D16 catalog’’ are very small.

3.1 Column density distribution function (CDDF):

Column density distribution function, $f(N_{\text{HI}}, z)$, describes the number of absorption lines in the column density range $\log N_{\text{HI}}$ and $\log N_{\text{HI}} + d\log N_{\text{HI}}$ and in the redshift range z to $z + dz$. For a singular isothermal density profile of Ly- α absorbers, the H I photoionization rate Γ_{HI} can be inferred from H I CDDF as (Schaye 2001; Shull et al. 2012),

$$f(N_{\text{HI}}, z) = \frac{\partial^2 N}{\partial z \partial \log(N_{\text{HI}})} \propto \Gamma_{\text{HI}}^{-1/2} \quad (5)$$

We take into account the completeness of the sample while calculating the redshift path length as a function of $\log N_{\text{HI}}$. Following D16, we calculate the CDDF in 13 $\log N_{\text{HI}}$ bins with centers at 12.5, 12.7, \dots , 14.7, 14.9 and width $d\log N_{\text{HI}} = 0.2$.

Left-hand panel in Fig. 4 illustrates the procedure we adopt for calculating the redshift path length. The top, middle and lower sub-panels show the flux F , SNR per pixel and equivalent width vector $W(\lambda)$ respectively for a sightline towards QSO H1821+643. To calculate the equivalent width vector $W(\lambda)$, Eq.4 is rearranged and solved for $W(\lambda)$ by taking $\text{RSL}=4$ and $b = 17 \text{ km s}^{-1}$ (corresponds velocity resolution) for each pixel. Next we calculate limiting equivalent width W_{lim} from curve of growth ($b = 17 \text{ km s}^{-1}$) for different values of $\log N_{\text{HI}}$. As an example we show W_{lim} for $\log N_{\text{HI}} = 12.5$ by black dashed horizontal line in bottom panel of Fig. 4. The redshift path length $\Delta z(N_{\text{HI}} = 10^{12.5} \text{ cm}^{-2})$ for this sightline (shown by blue curve in bottom panel) is the sum of redshift range for which $W(\lambda) \leq W_{\text{lim}}$. The total redshift path length $\Delta z(N_{\text{HI}})$ covered in the observed sample is a sum of all the redshift path length in individual sightlines. The total redshift path length $\Delta z(N_{\text{HI}})$ is then plotted as a function of $\log N_{\text{HI}}$ (‘‘Sensitivity curve’’) as shown in right-hand panel of Fig. 4. The completeness limit for the sample is $\log N_{\text{HI}} = 13.6$

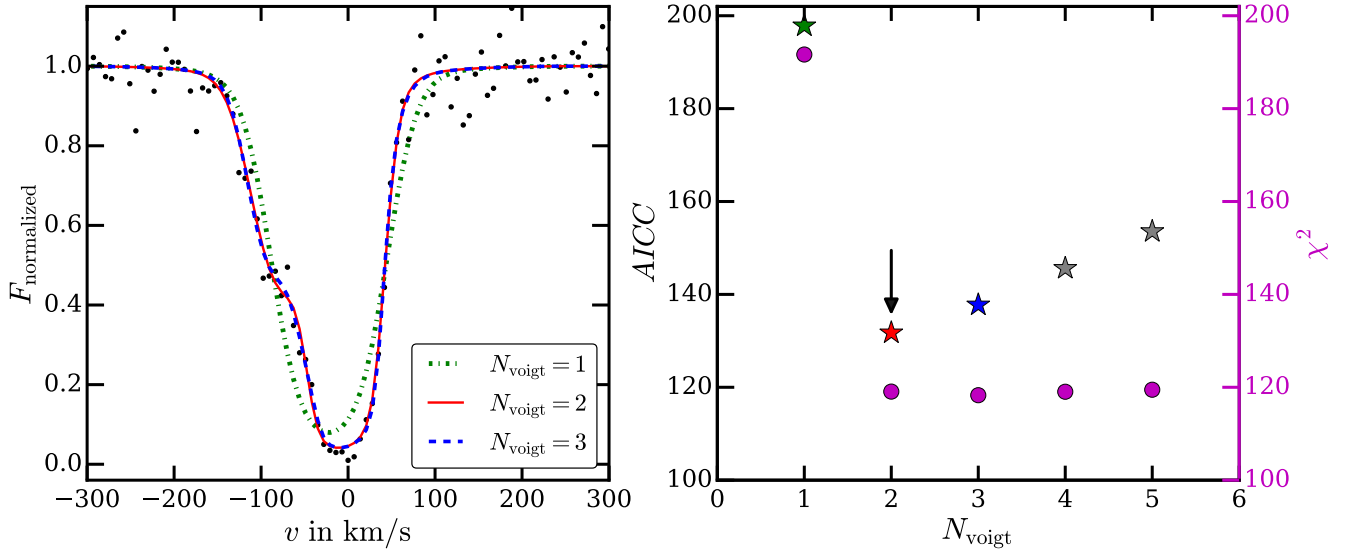


Figure 2. *Left-hand* panel shows the three different Voigt profile fits with $N_{\text{Voigt}} = 1, 2$ and 3 (green dot-dashed, red continuous and blue dashed lines respectively) fitted to the observed data (black circle). The spectrum is shown in the velocity scale defined with respect to the redshift of the strongest line center. *Right-hand* panel shows the corresponding variation of AICC (stars) and χ^2 (magenta circles) for 5 different models. For legibility fits with $N_{\text{Voigt}} = 4, 5$ (gray star points) are not shown in left-hand panel. For $N_{\text{Voigt}} > 2$, the χ^2 remains constant whereas AICC increases due to the second term on right-hand side of Eq.3. The best fit model corresponds to the minimum AICC (where $\chi_{\text{dof}}^2 \sim 1$ is also achieved) i.e., $N_{\text{Voigt}} = 2$ shown by black arrow in right-hand panel and red solid line in left-hand panel.

(shown by blue arrow) i.e., the lines with $\log N_{\text{HI}} \geq 13.6$ are always detectable over the entire observed wavelength range for the full sample. The fractional area $dA = dz \times d\log N_{\text{HI}}$ in Eq.5 is calculated by integrating the sensitivity curve in the corresponding $d\log N_{\text{HI}}$ bin. We shall refer to the CDDF obtained for our fitted parameters (over the redshift range $0.075 \leq z \leq 0.45$) in this way as “VIPER CDDF”.

In the left-hand panel of Fig. 5, we compared the VIPER CDDF with CDDF given in Table.5 of D16 (also S15) and CDDF calculated from D16 line catalog. The CDDF given in Table.5 of D16 is calculated from 2256 H I absorbers in the redshift range $0 \leq z < 0.75$ whereas CDDF calculated from D16 line catalog contains 1280 H I absorbers in the redshift range $0.075 \leq z < 0.45$. We used our redshift path length estimation for CDDF calculation from D16 line catalog. The VIPER and the D16 line catalog CDDFs are consistent with each other within 1σ except at high and low $\log N_{\text{HI}}$ bins. The median $\log N_{\text{HI}}$ from VIPER and D16 is 13.39 ± 0.61 and 13.38 ± 0.63 respectively. The two sample KS test p -value between the $\log N_{\text{HI}}$ distribution of VIPER and D16 line catalog is 0.83. The consistency between VIPER CDDF and D16 line catalog CDDF suggests that the number of components identified by VIPER in different $d\log N_{\text{HI}}$ bins are similar to those from D16 line catalog. Whereas, the agreement between VIPER CDDF and CDDF from D16 paper indicates that our redshift path calculation is consistent with that from D16 paper.

We notice occasional component differences when the Ly- α line is heavily saturated between D16 and our VIPER fits. Unlike D16, VIPER does not include simultaneous fitting of Ly- α line and higher order Lyman series lines (such as Ly- β , Ly- γ). This could be the reason for minor mismatch of CDDF in the bins $\log N_{\text{HI}} = 13.5 - 13.7$ and $\log N_{\text{HI}} = 14.7 - 14.9$. Thus minor differences one notices in high

and intermediate $\log N_{\text{HI}}$ bins in observed CDDF can be attributed to the differences in the multi-component fitting procedure in particular to the way the total number of components fitted to a given identified absorption region. However, there is an overall good agreement between CDDF derived by D16 and VIPER.

In the right-hand panel of Fig. 5, we compared the doppler- b parameter distribution from VIPER catalog (red curve with shaded region) and D16 line catalog (black dashed line with error bars)¹². In both distributions the errors are assumed to be poisson distributed. The median value of b parameter from VIPER and D16 is 32.9 ± 20.8 km s^{-1} and 33.9 ± 18.3 km s^{-1} respectively. The two sample KS test p -value between the b parameter distribution of VIPER and D16 line catalog is 0.41. Thus the two distributions are consistent with each other validating the consistency between VIPER and D16 line fitting methods.

4 SIMULATION

In this section we discuss the simulations used to generate the Ly- α forest that will be subsequently used to constrain Γ_{12} in §5. We used publicly available smoothed particle hydrodynamic code GADGET-2¹³ (Springel 2005) to generate density and velocity field in a periodic box of size $50 h^{-1}$ cMpc. The initial conditions were generated at $z = 99$ by

¹² In left-hand panel of Fig. 5, we compare our CDDF with that from D16 line catalog ($0.075 \leq z < 0.45$) and D16 paper ($0 \leq z < 0.75$). However, in right-hand panel of Fig. 5, we compare our b parameter distribution (i.e. in the redshift range $0.075 \leq z < 0.45$) with that from D16 catalog only as the b parameter distribution is not available in D16 paper.

¹³ <http://wwwmpa.mpa-garching.mpg.de/gadget/>

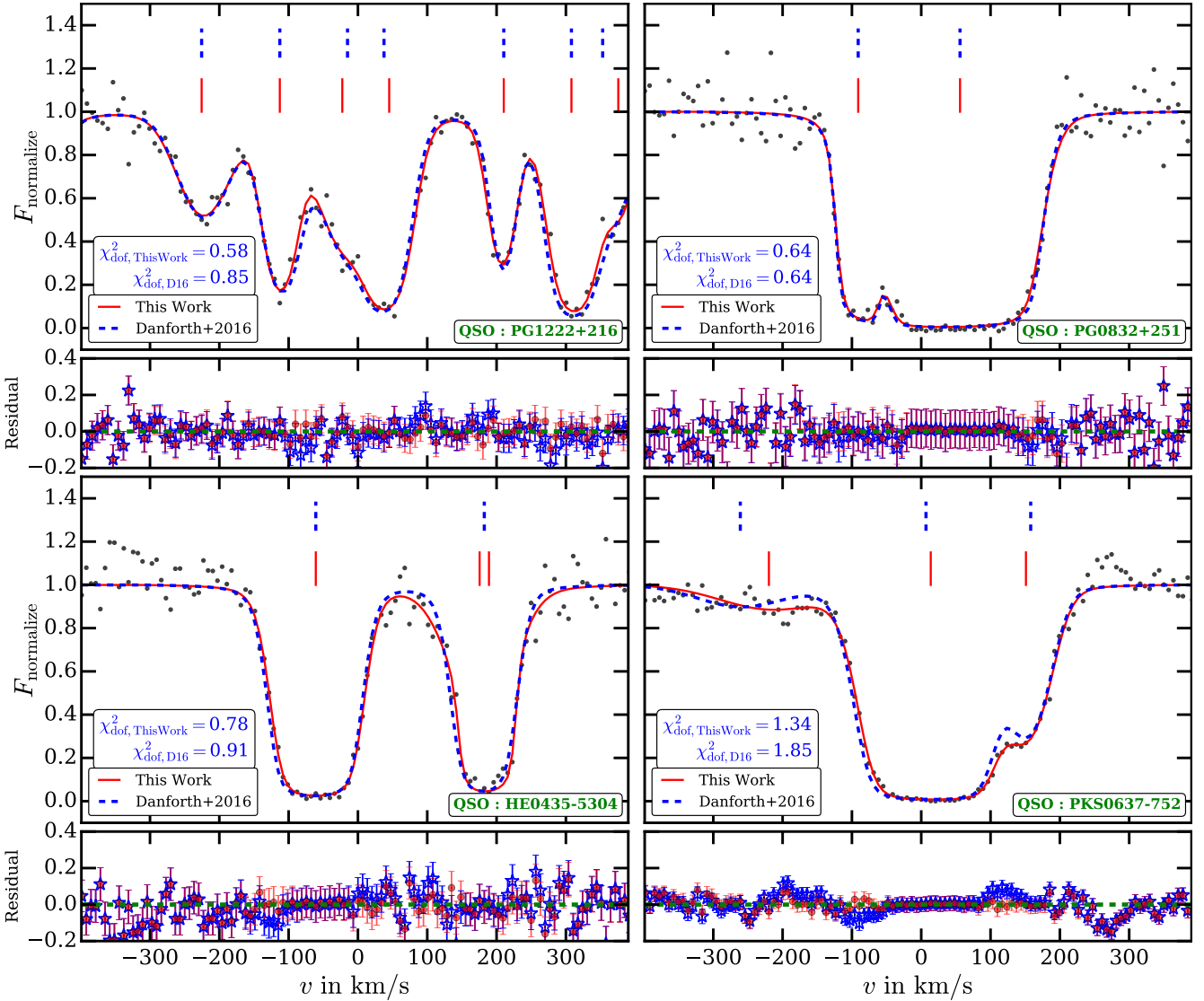


Figure 3. Comparison of Voigt profiles fitted using our procedure with those of D16 for four different regions in our sample. Black filled circles, the solid red line and the dashed blue line are observed data points, the best fit profile from VIPER and from D16 respectively. The spectra are shown in the velocity scale defined with respect to the redshift of the strongest component. Blue dashed and red continuous vertical ticks show the location of identified components by D16 and VIPER respectively. The residual between observed data and fitting from D16 (open blue stars) and VIPER (red filled circles) model are shown in the corresponding lower panel. In majority of cases (~ 89 percent, like upper row panels) our parameters within 1σ errors match with those from D16. However, for some cases our fit to the data using AICC (i.e., using criteria $\Delta\text{AICC} \geq 5$, see text for details) is found to be better (lower row panels). In all four cases shown above our χ^2_{dof} is better than the corresponding from D16.

using the publicly available 2LPT¹⁴ (Scoccimarro et al. 2012) initial conditions code. Radiative heating and cooling processes are not incorporated in default version of GADGET-2. We used our module “Code for Ionization and Temperature Evolution” (hereafter CITE) to evolve the temperature of the IGM in the post-processing step of the GADGET-2. We refer reader to Paper-I where CITE is discussed in detail.

In Paper-I, we showed the consistency of our method of evolving IGM temperature in GADGET-2+CITE with other low- z simulations in the past (Davé et al. 2010; Smith et al. 2011; Tepper-García et al. 2012) using 3 metrics (i)

the thermal history parameters at $z < 0.5$, (ii) distribution of baryons in different regions of the phase diagram and (iii) column density (N_{HI}) vs overdensity (Δ) relationship. We used model T15 – $\gamma 1.3$ given in Table 3 of Paper-I to calculate column density distribution function. In this model we evolve the equation of state of the IGM from $T_0 = 15000$ K and $\gamma = 1.3$ at $z = 2.1$ to $z = 0$. The final thermal history parameters at low redshift for this model are $(z, T_0, \gamma) \equiv (0.4, 5220, 1.51), (0.3, 4902, 1.53), (0.2, 4583, 1.54), (0.1, 4245, 1.55)$

Once we have calculated temperature of the GADGET-2 particles we generate the Ly- α forest by shooting random lines of sight through simulation box (Choudhury et al. 2001; Padmanabhan et al. 2015, Paper-I). To account for the pos-

¹⁴ <http://cosmo.nyu.edu/roman/2LPT/>

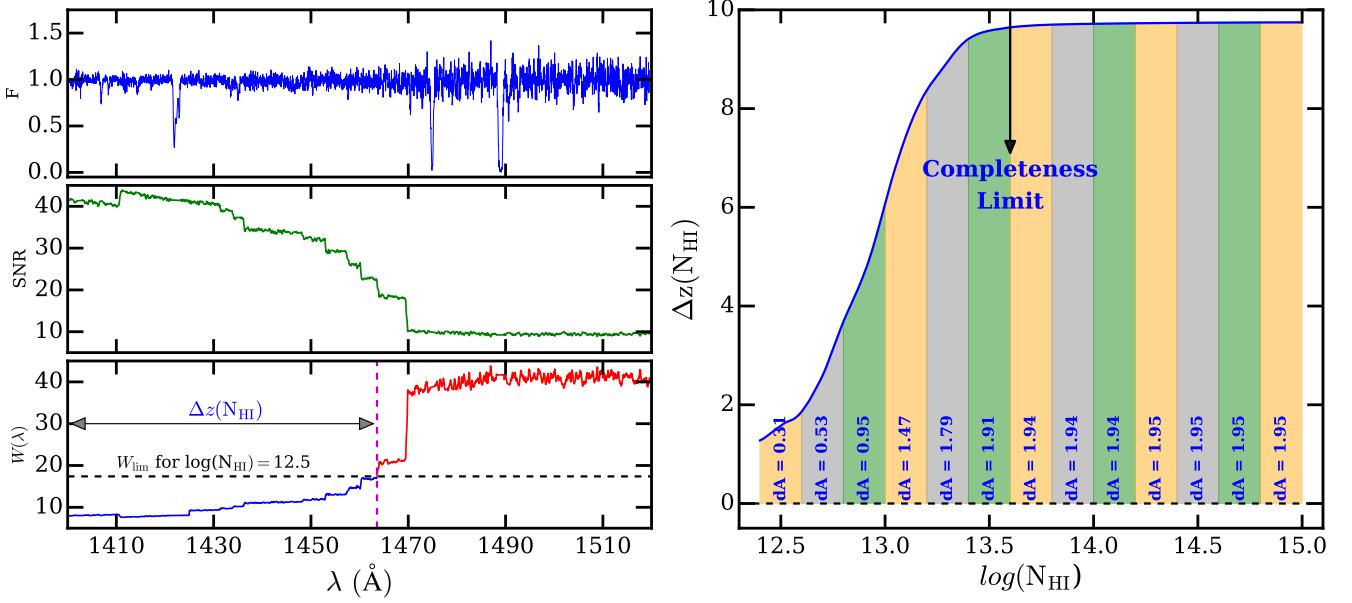


Figure 4. *Left-hand* panel illustrates our redshift path length calculation for sightline towards QSO H1821+643. Top, middle and lower left-hand panels show the flux, SNR per pixel and equivalent width vector respectively. Equivalent width vector $W(\lambda)$ is calculated for RSL = 4 in Eq.4. The limiting equivalent width (W_{lim}), estimated from the curve of growth, corresponding to $\log(N_{\text{HI}}) = 12.5$ is shown by horizontal black dashed line in the bottom panel. The redshift path length, $\Delta z(N_{\text{HI}} = 10^{12.5} \text{ cm}^{-2})$, for this sightline is the redshift covered by region $W(\lambda) \leq W_{\text{lim}}$. The total redshift path length is sum of the Δz measured along all QSO sightlines. *Right-hand* panel shows (blue curve) the total redshift path length as a function of $\log N_{\text{HI}}$ (known as sensitivity curve). The completeness limit for the sample is $\log N_{\text{HI}} = 13.6$ (shown by blue arrow). The fractional area in a given $\log N_{\text{HI}}$ bin, $dA = dz d\log(N_{\text{HI}})$, is area under the blue curve in the corresponding $\log N_{\text{HI}}$ bin (shown by blue text) that is used in CDDF calculation.

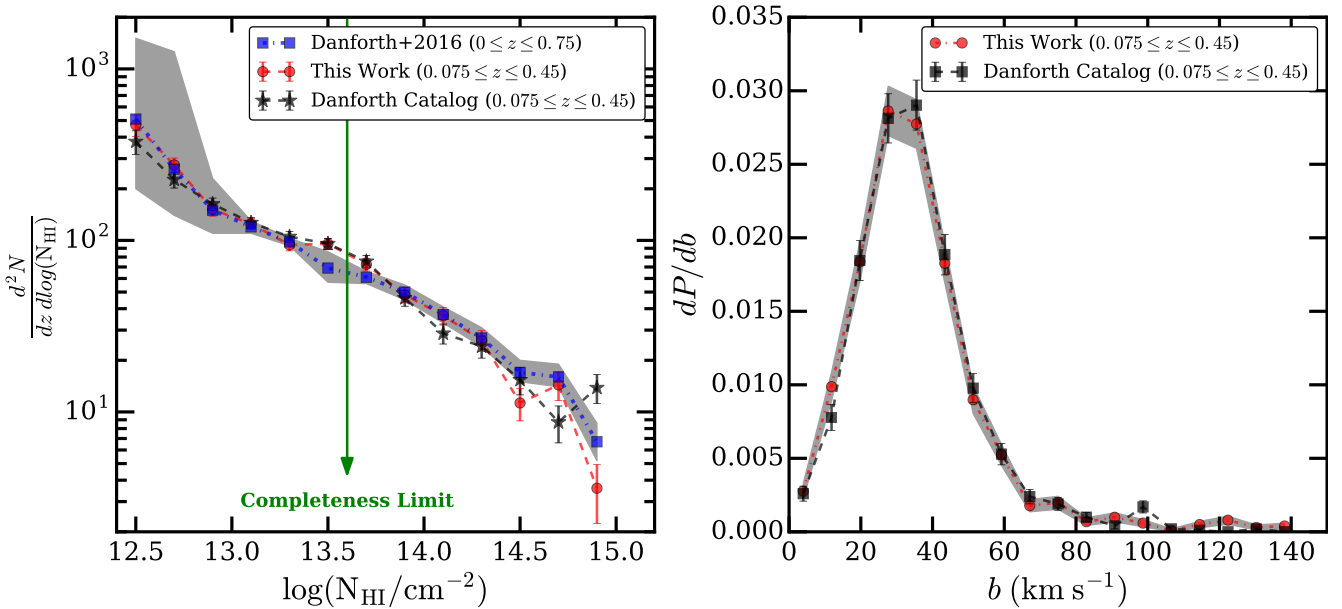


Figure 5. Left-hand panel shows comparison of CDDF from VIPER (red circle, $0.075 \leq z \leq 0.45$, 1277 H I Ly- α lines), D16 line catalog (black stars, for $0.075 \leq z \leq 0.45$, 1280 H I Ly- α lines) and Table.5 in D16 (blue square curve with gray shaded region, for $0 \leq z \leq 0.75$, 2256 H I Ly- α lines). The two sample KS test p -value between VIPER and D16 line catalog for $\log N_{\text{HI}}$ distribution is 0.83. Thus within errors the CDDF from the two methods are consistent with each other. At high column densities the differences arises due to differences in the fitting procedure (multi-component fitting using AICC). Right-hand panel shows the b parameter distribution from VIPER (red curve for $0.075 \leq z \leq 0.45$) and D16 line catalog (black curve with shaded region for $0.075 \leq z \leq 0.45$). The two sample KS test p -value between VIPER and D16 line catalog for b parameter distribution is 0.41. Thus the b parameter distribution from VIPER is in good agreement with that of D16 line catalog validating our procedure. In both panels the error bars shown are computed assuming the Poisson distribution.

sible redshift evolution of the structures, we generated Ly- α forest from the simulation box at $\bar{z} = 0.1, 0.2, 0.3$ and 0.4 for comparison with observations. The basic steps are as follows,

- Using SPH smoothing kernel, the density, velocity and temperature are calculated on the grids along the sightline.
- Assuming photoionization equilibrium with ultra-violet background (hereafter UVB), the number density of neutral hydrogen (n_{HI}) is calculated along the sightline.
- We treat H I photoionization rate (Γ_{HI}) as a free parameter in our analysis. For a given value of Γ_{12} , Ly- α optical depth τ is calculated at each pixel from the n_{HI} field and by properly accounting for peculiar velocity, thermal width and natural width effects on the line profile. The transmitted flux is then given by $F = \exp(-\tau)$.
- The velocity separation of pixels in the simulated spectra is $\sim 5 \text{ km s}^{-1}$ whereas observed spectra are at $\sim 17 \text{ km s}^{-1}$ velocity resolution. We linearly interpolate the simulated spectra to match with observed velocity resolution.
- The line spread function of HST-COS is skewed and has extended wings. We account for this effect by convolving the simulated spectra with HST-COS LSF. Finally we add the Gaussian random noise to the simulated spectra with SNR same as the observed spectra.

We generated $N \times N_{\text{spec}}$ number of Ly- α forest spectra at redshift z to account for the variance in the model CDDF (for similar method see Rollinde et al. 2013, Paper-I). Here, N_{spec} is number of observed spectra at the redshift of interest z and $N = 100$ is number of mock samples. It should be noted that the dynamical impact of diffuse IGM pressure is not modeled self-consistently in CITE. However, these effects are not important for low resolution ($\sim 50 \text{ ckpc}$) simulations presented in this work (see Paper-I for details). Our simulations do not contain any higher order (i.e., Ly- β , Ly- γ and onward) Lyman series lines for most of our analysis. However, we consider the contamination by higher order Lyman series (in particular Ly- β from $z = 0.6$) lines with the Ly- α line for the highest- z bin i.e., $z = 0.4$ (see Paper-I).

5 RESULTS

In this section we decomposed Ly- α forest spectra generated from GADGET-2 + CITE simulations into multiple Voigt profiles using VIPER. We formed a line catalog for each mock sample and obtained three distributions (i) b parameter distribution, (ii) b vs $\log N_{\text{HI}}$ distribution and (iii) CDDF. These distributions calculated from different mock samples are used to estimate the errors. We compare these distributions from simulations with those from observation. In particular, we used CDDF to constrain the Γ_{12} and its evolution in four different redshift bins.

5.1 b parameter distribution

The b parameter distribution calculated from Voigt profile fitting is sensitive to thermal history, the energy injected by various astrophysical processes in the form of heat and unknown turbulent motions in the IGM (Schaye et al. 1999, 2000; McDonald et al. 2001; Davé & Tripp 2001). Recently it has been found that the b parameters obtained from various

hydrodynamical simulations are typically smaller compared to those from the observations at low- z (Viel et al. 2016) though the thermal history parameters self-consistently obtained in these simulations agree well with each other. The b parameters from our simulation (GADGET-2 + CITE) are also found to be significantly smaller than the observed b parameters (see left-hand panel of Fig. 6). Thus to match the b parameter distribution, additional thermally and/or non-thermally broadened b parameter is required.

We found that the observed b parameter distribution can be matched with simulation by increasing the temperature of each pixel along sightline by a factor of 3. This increase in temperature would correspond to injection of the energy in the form of heat into the IGM. Increasing the gas temperature can lead to two effects (i) reducing the recombination rate coefficient as it scales as $\sim T^{-0.7}$ and (ii) introduce additional ionization due to collisions in the high density gas. By artificially enhancing the heating rate by more than a factor of 3, Viel et al. (2016) have recently shown the simulated b distribution can be made consistent with the observed ones. However such a model tends to suggest lower Γ_{HI} compared to simulations without additional heating (see Table 1 in Viel et al. 2016). As we will show in §5.4, a lower value of Γ_{HI} would imply that the number of ionizing photons in the IGM is less than that expected from only QSOs. Hence we rather focus on a scenario where the additional contribution to the line broadening arises from non-thermal motions. Here we explore this possibility by introducing turbulent motions that can simultaneously explain b parameter distributions and b vs $\log N_{\text{HI}}$ distributions as well.

In this work we incorporate additional broadening by adding a *non-thermal* (micro-turbulence) component b_{turb} to thermal b parameter in quadrature ($b^2 = b_{\text{thermal}}^2 + b_{\text{turb}}^2$) to mimic micro-turbulence that is missing in our simulation and see its effect on the derived Γ_{12} constraints. We refer to the non-thermal contribution to the b parameters as ‘micro-turbulence’, b_{turb} . In general, this ‘micro-turbulence’ is due to any physical phenomenon affecting the width of the absorption line that is not captured properly in our simulations e.g. various feedback processes and/or numerical effects¹⁵. Using this new b parameter we compute the Ly- α optical depth and fit each absorption line using VIPER to get b and $\log N_{\text{HI}}$. The Γ_{12} is then constrained from the model with and without micro-turbulence. We used two different models to quantify the micro-turbulence in simulation as explained below.

(i) Density dependent b_{turb} : In order to match the observed line width distribution of O VI absorbers, Oppenheimer & Davé (2009) added density dependent turbulence in their simulation. Following Eq. 5 and 6 given in Oppenheimer & Davé (2009), we added (in quadrature) the $b_{\text{turb}}(n_{\text{H}})$ in simulated spectra where n_{H} is hydrogen number density. The form of these equations is such that the contribution of the b_{turb} is appreciable only at high column densities i.e. $\log N_{\text{HI}} > 13.5$ (see middle panel in Fig. 7).

¹⁵ The physical phenomena occurring on scales below the resolution scale (i.e., below $\sim 50h^{-1} \text{ ckpc}$) of the simulation box may affect the scales that are resolved (Springel & Hernquist 2002). These physical phenomena may not be captured properly in the simulation box.

The b parameter distribution for this case is shown in the middle panel of Fig. 6. It is clear that the simulated b values are smaller than the observed ones even in this case.

(ii) Gaussian random b_{turb} : In this approach we generated b_{turb} from a Gaussian random variable with mean $\mu = 20 \text{ km s}^{-1}$ and standard deviation $\sigma = 10 \text{ km s}^{-1}$ at each grid point along a sightline in the simulation box¹⁶. These values are in agreement with the distribution of non-thermal broadening parameters (see Fig. 24 in Tripp et al. 2008; Muzahid et al. 2012) derived for the well-aligned O VI and H I absorbers. From Fig. 6 (right-hand panel), we see that the agreement between the observed and model b parameter distribution is better in the case of Gaussian distributed b_{turb} model than the other two models i.e., without any additional b_{turb} and density dependent b_{turb} models. The model results shown in Fig. 6 were based on simulations that use the best fitted redshift evolution of Γ_{12} as given in Paper-I. However, we also found that the b parameter distribution depends weakly on the assumed evolution of Γ_{HI} .

5.2 b vs $\log N_{\text{HI}}$ distribution

In this section we discuss the effect of adding b_{turb} on the b vs $\log N_{\text{HI}}$ 2D distribution¹⁷. Fig. 7 shows comparison of b vs $\log N_{\text{HI}}$ distribution ($0.075 \leq z \leq 0.45$) from observations (shown by magenta points) with that from 3 different models (i) without turbulence (left-hand panel), (ii) density dependent b_{turb} as suggested by Oppenheimer & Davé (2009, middle panel) and (iii) Gaussian distributed b_{turb} (right-hand panel). The color scheme indicates the density of points in logarithmic units. To assess the goodness-of-fit, we calculated the reduced χ^2 for 2D distribution by binning the data along b axis in 21 bins (with bin width 7.5 km s^{-1}) and along $\log N_{\text{HI}}$ axis in 13 bins (with bin width 0.2). Let $P_{\text{sim},k}(i, j)$ be the value of 2D distribution of k^{th} mock sample in i^{th} , j^{th} bin along $\log N_{\text{HI}}$, b axis respectively. The mean and standard deviation of 2D distribution from mock samples can be calculated as,

$$\begin{aligned} \bar{P}_{\text{sim}}(i, j) &= \frac{1}{N} \sum_{k=1}^N P_{\text{sim},k}(i, j) \\ \sigma_{\text{sim}}^2(i, j) &= \frac{1}{N-1} \sum_{k=1}^N [P_{\text{sim},k}(i, j) - \bar{P}_{\text{sim}}(i, j)]^2 \end{aligned} \quad (6)$$

where $N = 100$ is the number of mock samples. Let $P_{\text{obs}}(i, j)$ be the value of observed 2D distribution in i^{th} , j^{th} bin along $\log N_{\text{HI}}$, b axis respectively. Note that both distributions i.e., $P_{\text{obs}}(i, j)$ and $P_{\text{sim},k}(i, j)$ are normalized. The reduced χ^2 between the observed and model distribution is,

$$\chi_{\text{dof}}^2 = \frac{1}{N_y \times N_x - 1} \sum_{i=1}^{N_x} \sum_{j=1}^{N_y} \frac{[\bar{P}_{\text{sim}}(i, j) - P_{\text{obs}}(i, j)]^2}{\sigma_{\text{sim}}^2(i, j)} \quad (7)$$

¹⁶ We calculated b vs $\log N_{\text{HI}}$ for 5 different $(\mu, \sigma) \equiv (10, 10), (20, 5), (20, 10), (20, 15), (30, 10)$ combinations. The χ^2 is found to be minimum for $\mu = 20 \text{ km s}^{-1}$ and $\sigma = 10 \text{ km s}^{-1}$.

¹⁷ We refer reader to Webb & Carswell (1991); Fernández-Soto et al. (1996) for discussions on Voigt profile fitting procedure influencing this correlation.

where $N_x = 13$ and $N_y = 21$ is number of bins along $\log N_{\text{HI}}$ and b axis respectively. From Fig. 7 the χ_{dof}^2 for Gaussian distributed b_{turb} is better (~ 2.1) than the model without turbulence ($\chi_{\text{dof}}^2 \sim 4.2$) and model with density dependent b_{turb} ($\chi_{\text{dof}}^2 \sim 3.8$).

Another way to assess the goodness of the assumed form for b_{turb} is to match the lower-envelope in b vs $\log N_{\text{HI}}$ distribution. At $z > 2$, the lower envelope is strongly correlated with thermal history parameters and has been used in the past to measure the effective equation of state of the IGM at high- z (Schaye et al. 1999, 2000). The red stars with solid line and black circles with dashed line in Fig. 7 shows the lower envelope for observed and model b vs $\log N_{\text{HI}}$ distribution respectively. The lower envelope is obtained by calculating the 10th percentile of b values in each $\log N_{\text{HI}}$ bin (Garzilli et al. 2015). In model b vs $\log N_{\text{HI}}$ distribution, the lower envelope is calculated for all mock samples. The black circles with errorbars in Fig. 7 represents mean and standard deviation of lower envelope from mock samples. In the case of models without turbulence we see that the lower envelope obtained for the observed data is systematically higher than that from simulation for $\log N_{\text{HI}} \geq 13.2$. It is also clear from the middle panel that density dependent turbulence overproduce b at $\log N_{\text{HI}} > 14.2$ and under produce in the range $13 \leq \log N_{\text{HI}} \leq 14$. It is evident from Fig. 7 that the lower envelope in Gaussian distributed b_{turb} model (right-hand panel) matches well with the observed lower envelope at $\log N_{\text{HI}} \geq 13.2$ ¹⁸. At low column densities i.e., $\log N_{\text{HI}} < 13.2$ the observed b parameters tend to be smaller than what is predicted in this case. This suggests that the actual b_{turb} could be smaller at $\log N_{\text{HI}} < 13.2$ compared to mean value we have assumed. Note at these low $\log N_{\text{HI}}$ values Ly- α absorption are in the linear part of curve of growth and N_{HI} measurements are independent of b parameter.

In summary the Gaussian distributed b_{turb} model matches well with observation for b vs $\log N_{\text{HI}}$ distribution and b parameter distribution. We reemphasize that this may not be the unique explanation for the additional broadening required in the simulation even-though it consistently reproduces the b parameter distribution and b vs $\log N_{\text{HI}}$ scatter. In the next section, we calculate CDDF and constrain Γ_{12} from observation by comparing model with Gaussian distributed b_{turb} and model without any b_{turb} .

5.3 Γ_{HI} Constraints using CDDF

In this section we match model CDDF with the observed CDDF to constrain Γ_{12} in 4 redshift bins identified above. The CDDF is calculated for each mock sample. Γ_{12} is a free parameter in our analysis and the model CDDF depends on its value. The model CDDF is binned in a way identical to that of observed CDDF. Let $f_{\text{sim},i,k}(\Gamma_{12})$ be value of the CDDF in k^{th} bin of i^{th} mock sample for a given Γ_{12} . The mean and variance of CDDF in k^{th} bin is calculated as

¹⁸ The matching between observation and model with Gaussian distributed b_{turb} is also good when lower envelope is calculated using 5th and 20th percentile.

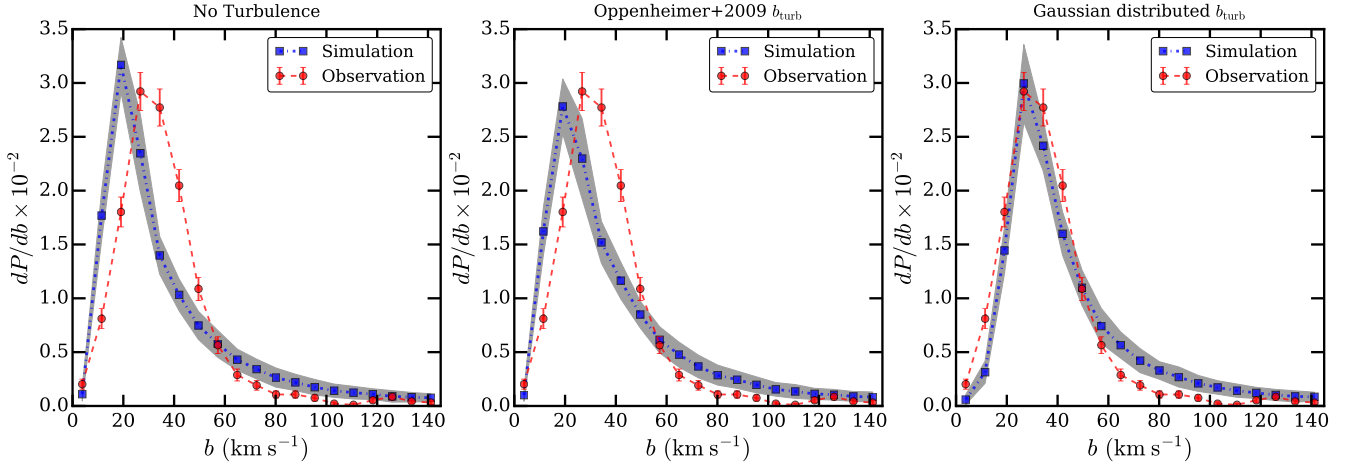


Figure 6. Comparison of b parameter distribution (at $0.075 \leq z \leq 0.45$) from observations (red dashed line with errorbar) and simulations (blue dotted line with 1σ shaded region) for 3 cases (see §5.1): (i) when b_{turb} is not added in the simulation (*left-hand panel*), (ii) when density dependent b_{turb} at given n_{HI} (Oppenheimer & Davé 2009) is added in the simulation (*middle panel*) and (iii) when Gaussian distributed b_{turb} is added in the simulation (*right-hand panel*). The errorbars on model b parameter distribution are calculated from mock sample whereas the errorbars on observed b parameter distribution are calculated assuming Poisson statistics. The b parameter distribution from models with Gaussian distributed b_{turb} qualitatively matches well with that from the observation.

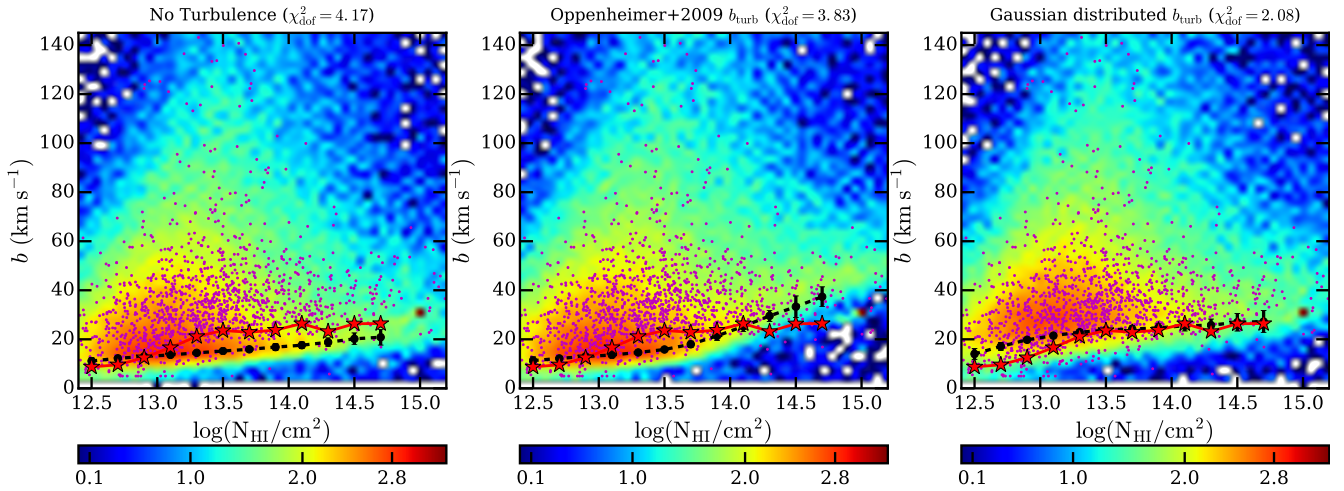


Figure 7. Comparison of b vs N_{HI} distribution (at $0.075 \leq z \leq 0.45$) from observation (magenta points) and simulation (color-coded diagram) for 3 cases (see §5.1) (i) when b_{turb} is not added in the simulation (*left-hand panel*), (ii) when density dependent b_{turb} at given n_{HI} (Oppenheimer & Davé 2009) is added in the simulation (*middle panel*) and (iii) when Gaussian distributed b_{turb} is added in the simulation (*right-hand panel*). The color scheme indicates density of points from the simulation in logarithmic units. The red solid line and black dashed line shows the lower envelope for observed and model data points in both panels. The lower envelope is obtained by calculating 10th percentile of b in $\log N_{\text{HI}}$ bins. The lower envelope matches well in the case where Gaussian distributed b_{turb} is added. We calculated the χ^2 between model and observation by binning the data into 2D bins. These values are quoted on top of each panel. The χ^2_{dof} is better for a model with Gaussian distributed b_{turb} ($\chi^2_{\text{dof}} = 2.08$) than a model without turbulence ($\chi^2_{\text{dof}} = 4.17$) and a model with density dependent b_{turb} ($\chi^2_{\text{dof}} = 3.83$).

follows.

$$\bar{f}_{\text{sim},k}(\Gamma_{12}) = \frac{1}{N} \sum_{i=1}^N f_{\text{sim},i,k}(\Gamma_{12}) \quad (8)$$

$$\sigma_{\text{sim},k}^2 = \frac{1}{N-1} \sum_{i=1}^N [f_{\text{sim},i,k}(\Gamma_{12}) - \bar{f}_{\text{sim},k}(\Gamma_{12})]^2$$

where $N = 100$ is number of mock samples. The reduced χ^2 between observed CDDF and model CDDF

is given as,

$$\chi^2_{\text{dof}}(\Gamma_{12}) = \frac{1}{N_{\text{bin}} - 1} \sum_{k=1}^{N_{\text{bin}}} \frac{[\bar{f}_{\text{sim},k}(\Gamma_{12}) - f_{\text{obs},k}]^2}{\sigma_{\text{sim},k}^2} \quad (9)$$

where $N_{\text{bin}} = 13$ is number of bins in CDDF and $f_{\text{obs},k}$ is observed CDDF in k^{th} bin.

Right-hand panels of Fig. 8 show the constraints on Γ_{12} from CDDF for a model without turbulence in the 4 different redshift bins. As expected the χ^2 curves are smooth parabolas with the minimum reduced ($\chi^2_{\text{dof},\text{min}} \sim 1.5$) as given in Table 1. The statistical uncertainty in Γ_{12} is shown

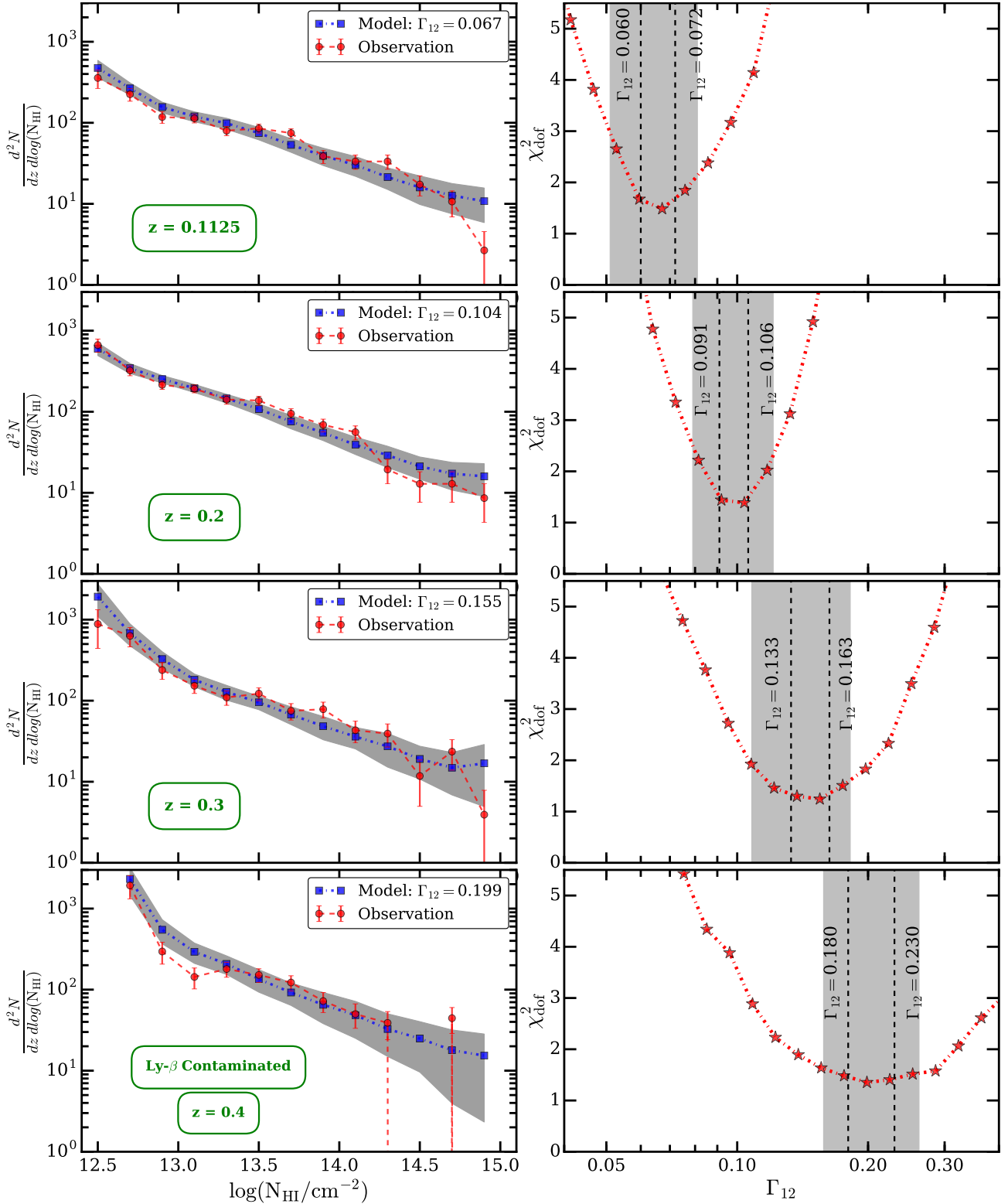


Figure 8. Constraints on Γ_{12} from CDDF in four different redshift bins. The *left-hand* panels show the observed CDDF and CDDF from the simulation using the best fitted Γ_{12} , i.e., Γ_{12} corresponding to the minimum reduced χ^2 , in different redshift bins (given in green box). The gray shaded region shows 1σ errorbar on the model CDDF (calculated from mock samples). The errors on observed CDDF (red line with errorbar) are obtained assuming poisson distribution and are not considered for calculating the reduced χ^2 . The *right-hand* panels show the reduced χ^2 as a function of the assumed Γ_{12} . The black dashed vertical lines indicate 1σ constraints on Γ_{12} around the Γ_{12} where reduced χ^2 is minimum. The shaded region indicates 1σ constraints on Γ_{12} from flux PDF and flux PS given in [Paper-I](#). The 1σ constraints on Γ_{12} from CDDF are well within those obtained using flux PDF and flux PS. The simulated Ly- α forest at $z = 0.4$ is contaminated by Ly- β forest from $z \sim 0.6$ in the same wavelength range to account for possible contamination due to intervening H I absorbers (see §5 for more details).

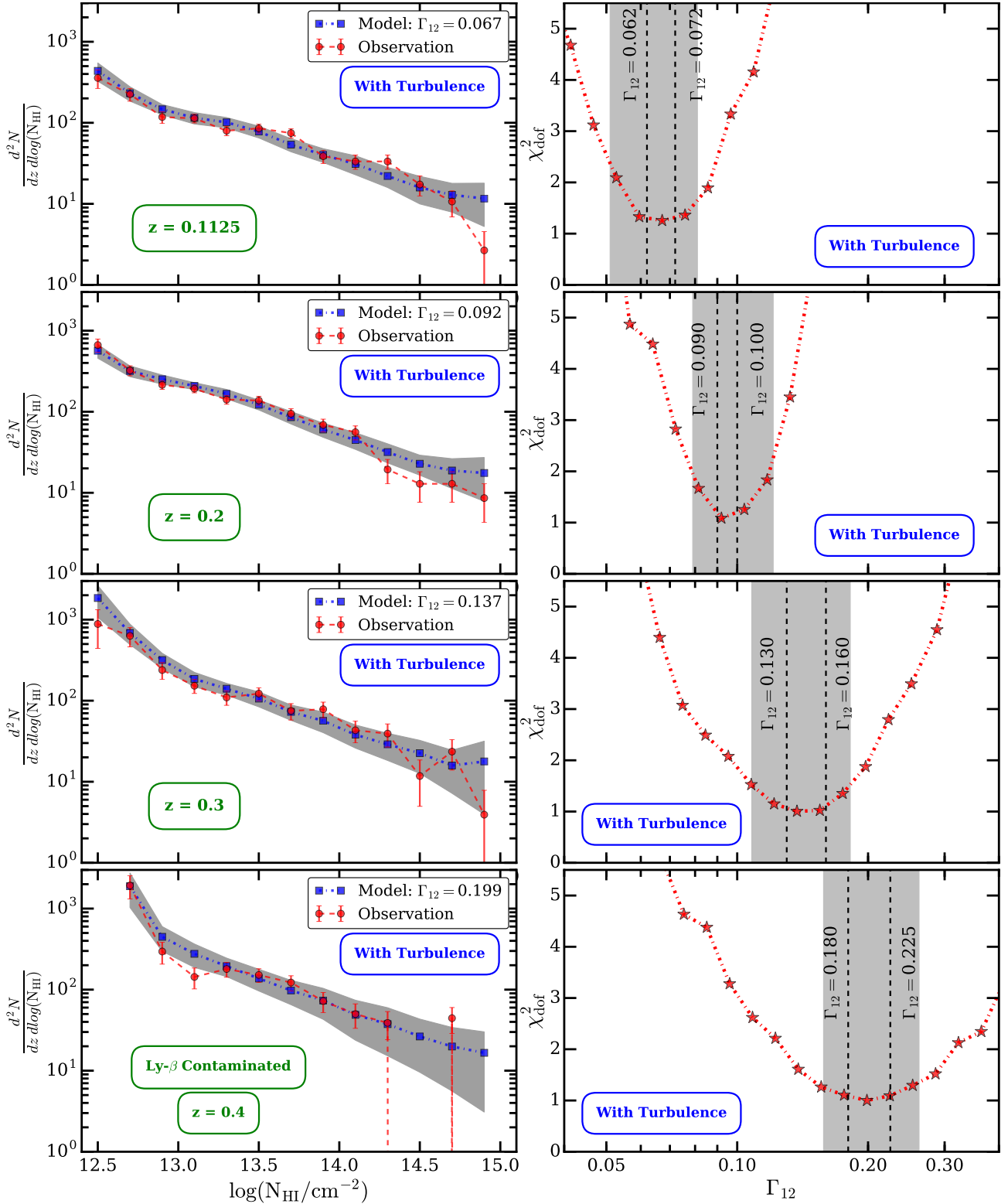


Figure 9. Same as Fig. 8 except Γ_{12} is constrained using a model with Gaussian distributed b_{turb} see §5.1.

by black dashed vertical line. The statistical uncertainty in Γ_{12} is calculated by demanding $\chi^2 = \chi^2_{\text{min}} + \Delta\chi^2$, where χ^2_{min} is minimum value of χ^2 and $\Delta\chi^2 = 1.0$ for 1 degree of freedom (corresponds to 1 free parameter in the problem i.e., Γ_{12} ; Press et al. 1992). The shaded regions shown in

the right-hand panels correspond to 1σ constraint on Γ_{12} from Paper-I. It is interesting to note that the Γ_{HI} constraints obtained using CDDF in this work (see Table 1) are consistent within $\sim 1\sigma$ (the best fit values differ by < 5.5 percent) with those obtained using flux statistics in Paper-I

(see Table 8 in [Paper-I](#)). However, error range is smaller in the present study. It is because, contrary to [Paper-I](#), here we do not consider the errors arising from uncertainties in cosmological parameters, continuum fitting and cosmic variance. Therefore, we caution the reader that errorbars on Γ_{12} from [Paper-I](#) are more realistic.

Left-hand panels in Fig. 8 shows the best fit (i.e., models with Γ_{12} corresponding to minimum χ^2_{dof}) model CDDF (blue square with shaded region) and observed CDDF (red circle with errorbar) in the 4 redshift bins. The gray shaded region represents 1σ range from the simulated mock sample (σ_{sim} given in Eq.8). The errorbars shown on observed CDDF are assumed to be poisson distributed and are not used while calculating χ^2 .

The redshift bin IV is likely to be affected by Ly- β contamination from H I interlopers (refer to [D16](#) and [Paper-I](#)). Note that it is difficult to remove the Ly- β contamination in observations due to limited wavelength coverage of the spectrograph. We accounted for this effect by contaminating the simulated Ly- α forest in the redshift $0.35 \leq z \leq 0.45$ with Ly- β forest from simulation box at $z = 0.6$. (for more detail we refer reader to §5.1 in [Paper-I](#)). The lowest panels in Fig. 8 shows the Γ_{12} constraint at $z = 0.4$ where model CDDF is calculated from Ly- α forest contaminated with Ly- β forest. The $\chi^2_{\text{dof, min}} = 1.35$ and Γ_{12} constraint are consistent (within 1σ) with best fit Γ_{12} from [Paper-I](#) (0.210 ± 0.052) in the same redshift bin¹⁹.

We have done similar analysis and constrained Γ_{12} for a model with Gaussian distributed b_{turb} (see §5.1) as shown in Fig. 9 (see Table 1 also). It is interesting to note that the Γ_{12} constraints obtained from the model with Gaussian distributed b_{turb} are in good agreement with those from model without turbulence and [Paper-I](#) (see left-hand panel in Fig. 10). This suggests that the addition of Gaussian distributed b_{turb} has a mild effect on CDDF (and hence Γ_{12} constraints). The $\chi^2_{\text{dof, min}}$ is also improved and close to 1 when Gaussian distributed b_{turb} is added to the model.

We summarize the best fit Γ_{12} (for the model with and without turbulence) along with the statistical errors for 4 redshift bins in Table 1. It is clear from left-hand panel of Fig. 10 that there is evolution in Γ_{12} with redshift and that follows $\Gamma_{\text{HI}}(z) = (3.9 \pm 0.1) \times 10^{-14} (1+z)^{4.98 \pm 0.11} \text{ s}^{-1}$ up to $z = 0.5$.

5.4 Implications of derived Γ_{HI} :

In this section we compare our derived Γ_{HI} with our previously measured Γ_{HI} from [Paper-I](#) and Γ_{HI} from the literature at low- z . Note previous studies (except [Paper-I](#)) do not get Γ_{HI} through χ^2 minimization and no errorbars are associated to the Γ_{HI} measurement. The Γ_{12} evolution from this work using CDDF for models with and without turbulence is in good agreement with Γ_{12} evolution (using flux PDF and flux PS) from [Paper-I](#). The uncertainty in Γ_{12} constraint from [Paper-I](#) is larger and more reliable as they also account for other systematic and statistical uncertainties.

Right-hand panel in Fig. 10 shows that our derived Γ_{12}

(0.066 ± 0.06) at $z = 0.1$ is lower than Γ_{12} from [K14](#) (~ 0.178) by factor ~ 2.7 but is consistent with [S15](#) (~ 0.070) within 1σ . [K14](#) compared the CDDF in the redshift range $0 \leq z \leq 0.75$ with models generated from simulation box at $z_{\text{sim}} = 0.1$. This could be the possible reason for the discrepancy of Γ_{12} constraints obtained in this work and [K14](#). We constrained Γ_{12} from CDDF in $0.075 \leq z \leq 0.45$ using models generated from simulation box at $z_{\text{sim}} = 0.1$ ignoring evolution in Γ_{12} and large scale structures. The Γ_{12} constraint (0.092 ± 0.009) for this model is higher by factor ~ 1.4 as compare to Γ_{12} constraint from the model at $z = 0.1$ where Γ_{12} evolution is accounted for (see Table 1). However, the Γ_{12} constraint from this model is in good ($\sim 1\sigma$) agreement with Γ_{12} constraint at $z = 0.2$ (0.104 ± 0.008 , see Table 1) when Γ_{12} evolution is accounted for. This is still smaller than what was found by [K14](#). Note that the median redshift of the observed sample is $z \sim 0.2$. Thus even if we do not account for Γ_{12} evolution, the Γ_{12} constraints (0.092 ± 0.009) are consistent with [S15](#) (~ 0.103 at $z = 0.2$) and [Paper-I](#) (0.100 ± 0.021 at $z = 0.2$).

Recently, [Gurvich et al. \(2016\)](#) found that the Γ_{12} required to match observed CDDF (from [D16](#)) with simulated CDDF is lower than [K14](#) by a factor ~ 3 . They attributed this to the effect of AGN feedback and to the [Faucher-Giguère et al. \(2009\)](#) UVB model included in their simulation. The AGN feedback could be important but is not incorporated in our simulation. However our Γ_{12} constraints are in good agreement with those from [Gurvich et al. \(2016\)](#). Note that our Γ_{12} constraint at $z = 0$ ($\Gamma_{12} = 0.039 \pm 0.001$, from scaling relation) is consistent within 1σ with that from [Faucher-Giguère et al. \(2009\)](#) UVB model ($\Gamma_{12} = 0.0384$). [Viel et al. \(2016\)](#) have provided scaled Γ_{12} for different hydrodynamical simulations with and without additional heating that will reproduce the observed CDDF. The direct comparison between our Γ_{12} measurements and that of [Viel et al. \(2016\)](#) is difficult as goodness of the CDDF fits and error in Γ_{12} are not given in their work. However if we assign 10 percent uncertainty to their measurements, they are very much in agreement with our measurements. [Cristiani et al. \(2016\)](#) found a similar result where their estimated Γ_{12} evolution at $z < 0.5$ is in good agreement with Γ_{12} evolution from [S15](#) and [Paper-I](#). [Cristiani et al. \(2016\)](#) combined the information from measured QSO contribution to cosmic UVB in the range $3.6 < z < 4.0$ with QSO luminosity function and estimated the production of ionizing photons from QSOs at various epoch ($0 \leq z \leq 5$).

We compare our measured Γ_{HI} with the UVB model. We find that the UVB generated using updated QSO emissivity ([Khaire & Srianand 2015a](#)) is in very good agreement with our Γ_{HI} measurements. The gray shaded region in right-hand side of Fig. 10 shows the Γ_{HI} obtained using this UVB model. This shaded region accounts for two different H I distributions (from [Haardt & Madau 2012](#); [Inoue et al. 2014](#)) and spectral energy distributions of QSOs ([Stevens et al. 2014](#); [Lusso et al. 2014](#)) used in the UVB models. Γ_{HI} measurements can be used to place constraints on escape fraction (f_{esc}) of the H I ionizing photons from galaxies (see [Inoue et al. 2006](#); [Khaire et al. 2016](#)). Using Γ_{HI} measured here and uncertainties on it from [Paper-I](#), we find that the f_{esc} is negligible (with star formation history from [Khaire & Srianand 2015b](#), the 3σ limits are 0.8 percent), consistent with measurements of average f_{esc} from low- z galaxies

¹⁹ If we do not account for Ly- β contamination, the Γ_{12} constraint is underestimated, a result similar to [Paper-I](#). For Ly- α forest only simulation at $z = 0.4$, $\Gamma_{12} = 0.176 \pm 0.013$

(Cowie et al. 2009; Bridge et al. 2010; Siana et al. 2010; Rutkowski et al. 2016). Therefore, low- z UVB is predominantly contributed by QSOs.

6 SUMMARY

In this work we constrain the H I photoionization rate Γ_{HI} and its redshift evolution at $z < 0.45$ from a sample of 82 QSO obtained from Cosmic Origins Spectrograph on board Hubble Space Telescope using H I column density distribution function (CDDF). To explore full Γ_{HI} range we have developed a code “Voigt profile Parameter Estimation Routine (VIPER)” to automatically fit the Ly- α absorption lines with Voigt profile. This code is parallel and is written in *python*. The main results of this work are as follows

- We fitted all the observed Ly- α forest spectra using VIPER and compiled a Ly- α line catalog called “VIPER line catalog”. The fitted parameters such as column density (N_{HI}), line width parameter (b) and line width distribution from VIPER line catalog are found to be consistent with those from Danforth et al. (2016). The median b parameter from VIPER ($32.9 \pm 20.8 \text{ km s}^{-1}$) is consistent with that from Danforth et al. (2016, $33.9 \pm 18.3 \text{ km s}^{-1}$). Whereas, the median $\log N_{\text{HI}}$ from VIPER (13.39 ± 0.61) is in good agreement with that from Danforth et al. (2016, 13.38 ± 0.63)

- We calculate the appropriate redshift path length $\Delta z(N_{\text{HI}})$ and the sensitivity curve from HST-COS data. We calculate the CDDF after accounting for the incompleteness of the sample. Our calculated CDDF in the redshift range ($0.075 \leq z \leq 0.45$) is consistent (KS test p -value is 0.83) with that of Danforth et al. (2016) CDDF in the redshift range ($0 \leq z \leq 0.75$).

- We found that the b parameters of Voigt profile components from simulations are typically underestimated as compared to observations. This difference can be rectified by including the Gaussian distributed line width parameter b_{turb} ($\mu = 20 \text{ km s}^{-1}$ and $\sigma = 10 \text{ km s}^{-1}$) at each pixel in the simulation. The resulting line width distribution from simulations matches roughly with observed line width distribution, scatter and lower envelope of the b vs $\log N_{\text{HI}}$ distribution. However, the CDDF has little effect of additional b_{turb} (< 7 percent) and the Γ_{HI} constraints are mildly affected (< 9 percent). However, if we consider additional heating effect for the excess broadening then the Γ_{HI} obtained will be slightly reduced (roughly scale as $T^{-0.7}$).

- We obtained CDDF at four different z bins and matched with simulated CDDF at each mean z . This allowed us to measure the Γ_{HI} in four redshift bins (of $\Delta z = 0.1$) centered around $\bar{z} = 0.1125, 0.2, 0.3, 0.4$. We estimated the associated statistical error using χ^2 statistics. When additional turbulent broadening are not included measured Γ_{12} values at the redshift bins $\bar{z} = 0.1125, 0.2, 0.3, 0.4$ are $\Gamma_{12} = 0.066 \pm 0.006, 0.104 \pm 0.008, 0.137 \pm 0.015, 0.199 \pm 0.025$ respectively. The corresponding values after inclusion of b_{turb} are $\Gamma_{12} = 0.067 \pm 0.005, 0.095 \pm 0.005, 0.145 \pm 0.015, 0.200 \pm 0.022$. Thus the uncertainties in the velocity broadening seem to have little effect on the derived Γ_{HI} . Our measured Γ_{12} values are in good agreement with Gaikwad et al. (2017) Γ_{12} measurement that are obtained with two different statistics namely flux PDF and flux PS. However, the errorbars on

Γ_{HI} measurements of Gaikwad et al. (2017) are more reliable as they account for cosmic variance, continuum fitting uncertainty and cosmological parameter uncertainty in their calculation.

- Our measured Γ_{HI} is increasing with z and follows the relation $\Gamma_{\text{HI}}(z) = (3.9 \pm 0.1) \times 10^{-14} (1+z)^{4.98 \pm 0.11} \text{ s}^{-1}$ which is in agreement with Shull et al. (2015). The measured Γ_{HI} evolution is consistent with Khaire & Srianand (2015a,b) UV background model where it is contributed only by QSOs (i.e., the galaxy contribution is negligible). Inclusion of additional thermal broadening will reduce the Γ_{HI} value obtained. This will further reduce the galaxy contribution to the Γ_{HI} at low- z .

ACKNOWLEDGMENT

All the computations were performed using the PERSEUS cluster at IUCAA and the HPC cluster at NCRA. We would like to thank Volker Springel, Matteo Viel and Simeon Bird for useful discussion. We also like to thank the referee John Webb and Matthew Bainbridge for improving this work and manuscript.

REFERENCES

- Akaike H., 1974, *IEEE Transactions on Automatic Control*, **19**, 716
- Armstrong B., 1967, *Journal of Quantitative Spectroscopy and Radiative Transfer*, **7**, 61
- Bainbridge M. B., Webb J. K., 2016, preprint, ([arXiv:1606.07393](https://arxiv.org/abs/1606.07393))
- Becker G. D., Bolton J. S., 2013, *MNRAS*, **436**, 1023
- Becker G. D., Bolton J. S., Haehnelt M. G., Sargent W. L. W., 2011, *MNRAS*, **410**, 1096
- Bi H., 1993, *ApJ*, **405**, 479
- Bi H., Davidsen A. F., 1997, *ApJ*, **479**, 523
- Bi H. G., Boerner G., Chu Y., 1992, *A&A*, **266**, 1
- Bolton J. S., Haehnelt M. G., 2007, *MNRAS*, **382**, 325
- Bolton J. S., Haehnelt M. G., Viel M., Springel V., 2005, *MNRAS*, **357**, 1178
- Bolton J. S., Viel M., Kim T.-S., Haehnelt M. G., Carswell R. F., 2008, *MNRAS*, **386**, 1131
- Bridge C. R., et al., 2010, *ApJ*, **720**, 465
- Calura F., Tescari E., D’Odorico V., Viel M., Cristiani S., Kim T.-S., Bolton J. S., 2012, *MNRAS*, **422**, 3019
- Cen R., Miralda-Escudé J., Ostriker J. P., Rauch M., 1994, *ApJ*, **437**, L9
- Choudhury T. R., Srianand R., Padmanabhan T., 2001, *ApJ*, **559**, 29
- Cooke A. J., Espey B., Carswell R. F., 1997, *MNRAS*, **284**, 552
- Cooke R. J., Pettini M., Jorgenson R. A., Murphy M. T., Steidel C. C., 2014, *ApJ*, **781**, 31
- Cowie L. L., Barger A. J., Trouille L., 2009, *ApJ*, **692**, 1476
- Cristiani S., Serrano L. M., Fontanot F., Vanzella E., Monaco P., 2016, *MNRAS*, **462**, 2478
- Croft R. A. C., Weinberg D. H., Katz N., Hernquist L., 1997, *ApJ*, **488**, 532
- Croft R. A. C., Weinberg D. H., Katz N., Hernquist L., 1998, *ApJ*, **495**, 44
- Danforth C. W., et al., 2016, *ApJ*, **817**, 111
- Davé R., Tripp T. M., 2001, *ApJ*, **553**, 528
- Davé R., Oppenheimer B. D., Katz N., Kollmeier J. A., Weinberg D. H., 2010, *MNRAS*, **408**, 2051
- Faucher-Giguère C.-A., Lidz A., Hernquist L., Zaldarriaga M., 2008, *ApJ*, **682**, L9

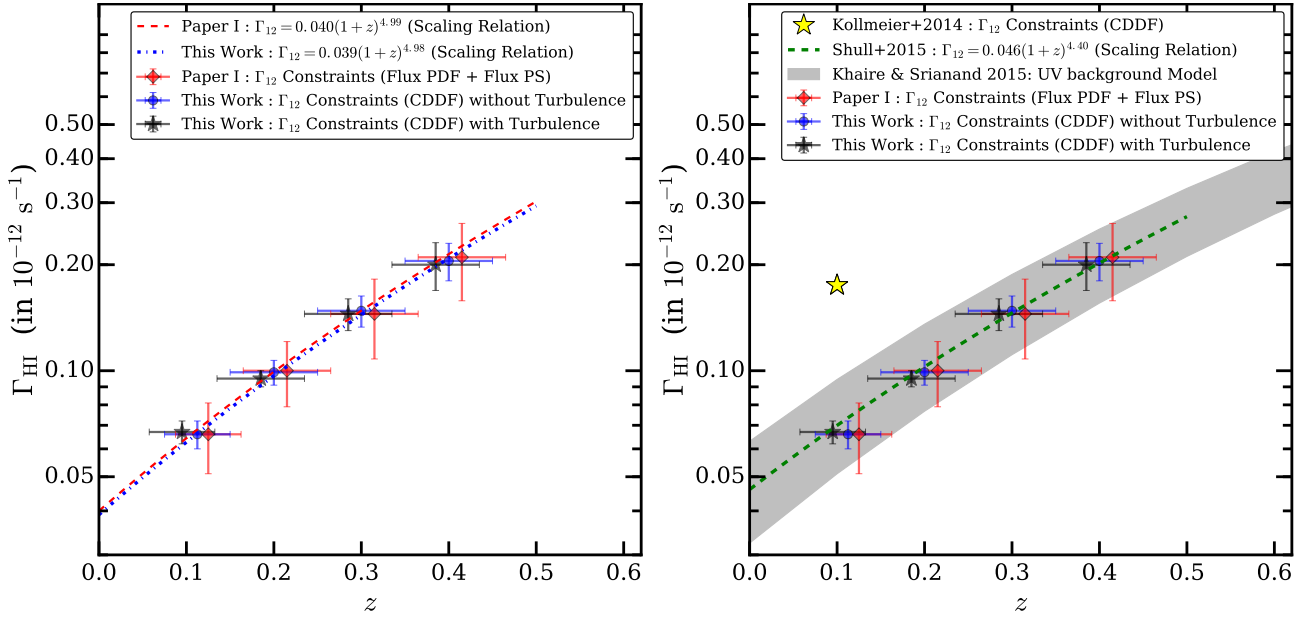


Figure 10. In the left-hand panel black stars and blue circles with errorbar show the evolution of Γ_{12} from this work (CDDF) for a model with turbulence (see §5.1) and without turbulence respectively. Red diamonds with errorbars show the Γ_{12} evolution from *Paper-I* (using flux PDF and flux PS). For visual purpose the points are shifted along x axis. The blue dotted and red dashed line shows scaling relation for Γ_{12} evolution from this work (for model without turbulence) and *Paper-I*. Within 1σ uncertainty the Γ_{12} evolution from this work (for both models with and without turbulence) is consistent with that from *Paper-I*. The errorbars on Γ_{12} evolution given in *Paper-I* are more realistic as they account for cosmic variance, cosmological parameter uncertainty, continuum fitting uncertainty. In the right-hand panel black stars, blue circles and red diamonds with errorbars are same as given in left-hand panel. Our derived Γ_{12} at $z \sim 0.1$ is lower by factor ~ 2.7 than that of *K14* (shown by yellow star) but is in 1σ agreement with *S15* (green dashed line). The derived Γ_{HI} evolution is consistent with *Khaire & Srianand (2015a,b)* UVB model (shown by gray shaded region) where the UVB is contributed only by QSOs.

Table 1. Γ_{12} measurements at different redshifts

Redshift bin \Rightarrow	I	II	III	IV
Type of simulated spectra \Rightarrow	Ly- α forest	Ly- α forest	Ly- α forest	Ly- α + Ly- β forest ¹
Best Fit Γ_{12} (without turbulence)	0.066	0.104	0.137	0.199
Statistical uncertainty ²	± 0.006	± 0.008	± 0.015	± 0.025
Reduced χ_{min}^2	1.49	1.39	1.24	1.35
Best Fit Γ_{12} (for Gaussian b_{turb})	0.067	0.095	0.145	0.200
Statistical uncertainty ²	± 0.005	± 0.005	± 0.015	± 0.022
Reduced χ_{min}^2	1.26	1.09	1.04	1.00

¹ Following *Paper-I*, simulated Ly- α forest at $z = 0.35$ to 0.45 is contaminated by Ly- β forest in the same wavelength range. The Ly- β forest is generated from simulation box at $z = 0.6$.

² The uncertainty in Γ_{12} due to uncertainty in thermal history parameters is well within statistical uncertainty.

Faucher-Giguère C.-A., Lidz A., Zaldarriaga M., Hernquist L., 2009, *ApJ*, **703**, 1416
 Fernández-Soto A., Lanzetta K. M., Barcons X., Carswell R. F., Webb J. K., Yahil A., 1996, *ApJ*, **460**, L85
 Gaikwad P., Khaire V., Choudhury T. R., Srianand R., 2017, *MNRAS*, **466**, 838
 Garzilli A., Theuns T., Schaye J., 2015, *MNRAS*, **450**, 1465
 Gurvich A., Burkhardt B., Bird S., 2016, preprint, ([arXiv:1608.03293](https://arxiv.org/abs/1608.03293))
 Haardt F., Madau P., 2012, *ApJ*, **746**, 125
 Hernquist L., Katz N., Weinberg D. H., Miralda-Escudé J., 1996, *ApJ*, **457**, L51
 Inoue A. K., Iwata I., Deharveng J.-M., 2006, *MNRAS*, **371**, L1

Inoue A. K., Shimizu I., Iwata I., Tanaka M., 2014, *MNRAS*, **442**, 1805
 Jeffreys H., 1961, *Theory of Probability*. 3rd edn. Oxford Univ. Press, Oxford
 Keeney B. A., Danforth C. W., Stocke J. T., France K., Green J. C., 2012, *PASP*, **124**, 830
 Khaire V., Srianand R., 2015a, *MNRAS*, **451**, L30
 Khaire V., Srianand R., 2015b, *ApJ*, **805**, 33
 Khaire V., Srianand R., Choudhury T. R., Gaikwad P., 2016, *MNRAS*, **457**, 4051
 King J. A., Murphy M. T., Ubachs W., Webb J. K., 2011, *MNRAS*, **417**, 3010
 Kollmeier J. A., et al., 2014, *ApJ*, **789**, L32

Liddle A. R., 2007, *MNRAS*, **377**, L74

Lidz A., Faucher-Giguère C.-A., Dall’Aglio A., McQuinn M., Fechner C., Zaldarriaga M., Hernquist L., Dutta S., 2010, *ApJ*, **718**, 199

Lusso E., et al., 2014, *ApJ*, **784**, 176

McDonald P., Miralda-Escudé J., Rauch M., Sargent W. L. W., Barlow T. A., Cen R., Ostriker J. P., 2000, *ApJ*, **543**, 1

McDonald P., Miralda-Escudé J., Rauch M., Sargent W. L. W., Barlow T. A., Cen R., 2001, *ApJ*, **562**, 52

McDonald P., et al., 2005, *ApJ*, **635**, 761

McQuinn M., Hernquist L., Lidz A., Zaldarriaga M., 2011, *MNRAS*, **415**, 977

Meiksin A., White M., 2004, *MNRAS*, **350**, 1107

Miralda-Escudé J., Cen R., Ostriker J. P., Rauch M., 1996, *ApJ*, **471**, 582

Muzahid S., Srianand R., Bergeron J., Petitjean P., 2012, *MNRAS*, **421**, 446

Oppenheimer B. D., Davé R., 2009, *MNRAS*, **395**, 1875

Padmanabhan H., Srianand R., Choudhury T. R., 2015, *MNRAS*, **450**, L29

Penton S. V., Shull J. M., Stocke J. T., 2000, *ApJ*, **544**, 150

Phillips J., Weinberg D. H., Croft R. A. C., Hernquist L., Katz N., Pettini M., 2001, *ApJ*, **560**, 15

Planck Collaboration et al., 2015, preprint, ([arXiv:1502.01589](https://arxiv.org/abs/1502.01589))

Pontzen A., Bird S., Peiris H., Verde L., 2014, *ApJ*, **792**, L34

Press W. H., Teukolsky S. A., Vetterling W. T., Flannery B. P., 1992, Numerical recipes in FORTRAN. The art of scientific computing

Rauch M., et al., 1997, *ApJ*, **489**, 7

Rollinde E., Theuns T., Schaye J., Pâris I., Petitjean P., 2013, *MNRAS*, **428**, 540

Rutkowski M. J., et al., 2016, *ApJ*, **819**, 81

Schaye J., 2001, *ApJ*, **559**, 507

Schaye J., Theuns T., Leonard A., Efstathiou G., 1999, *MNRAS*, **310**, 57

Schaye J., Theuns T., Rauch M., Efstathiou G., Sargent W. L. W., 2000, *MNRAS*, **318**, 817

Schneider D. P., et al., 1993, *ApJS*, **87**, 45

Scoccimarro R., Hui L., Manera M., Chan K. C., 2012, *Phys. Rev. D*, **85**, 083002

Seljak U., Slosar A., McDonald P., 2006, *J. Cosmology Astropart. Phys.*, **10**, 014

Shull J. M., Smith B. D., Danforth C. W., 2012, *ApJ*, **759**, 23

Shull J. M., Moloney J., Danforth C. W., Tilton E. M., 2015, *ApJ*, **811**, 3

Siana B., et al., 2010, *ApJ*, **723**, 241

Smith B. D., Hallman E. J., Shull J. M., O’Shea B. W., 2011, *ApJ*, **731**, 6

Springel V., 2005, *MNRAS*, **364**, 1105

Springel V., Hernquist L., 2002, *MNRAS*, **333**, 649

Stevens M. L., Shull J. M., Danforth C. W., Tilton E. M., 2014, *ApJ*, **794**, 75

Storrie-Lombardi L. J., McMahon R. G., Irwin M. J., 1996, *MNRAS*, **283**, L79

Tegmark M., et al., 2004, *ApJ*, **606**, 702

Tepper-García T., Richter P., Schaye J., Booth C. M., Dalla Vecchia C., Theuns T., 2012, *MNRAS*, **425**, 1640

Tripp T. M., Sembach K. R., Bowen D. V., Savage B. D., Jenkins E. B., Lehner N., Richter P., 2008, *ApJS*, **177**, 39

Viel M., Haehnelt M. G., 2006, *MNRAS*, **365**, 231

Viel M., Haehnelt M. G., Springel V., 2004a, *MNRAS*, **354**, 684

Viel M., Weller J., Haehnelt M. G., 2004b, *MNRAS*, **355**, L23

Viel M., Haehnelt M. G., Lewis A., 2006, *MNRAS*, **370**, L51

Viel M., Bolton J. S., Haehnelt M. G., 2009, *MNRAS*, **399**, L39

Viel M., Haehnelt M. G., Bolton J. S., Kim T.-S., Puchwein E., Nasir F., Wakker B. P., 2016, preprint, ([arXiv:1610.02046](https://arxiv.org/abs/1610.02046))

Webb J. K., Carswell R. F., 1991, in Shaver P. A., Wampller E. J., Wolfe A. M., eds, Quasar Absorption Lines. p. 3

Table 2. Few fitted parameters from the VIPER line catalog are given for spectra towards QSO 1ES1553+113. The full line catalog is available online in ASCII format.

λ (Å)	$d\lambda$ (Å)	$\log N_{\text{HI}}$ (cm^{-2})	$d\log N_{\text{HI}}$ (cm^{-2})	b (km s^{-1})	db (km s^{-1})
1330.827	0.003	13.68	0.01	32.06	1.08
1339.936	0.002	14.23	0.01	38.09	0.80
1361.466	0.019	12.84	0.06	34.10	7.00
1361.922	0.013	12.94	0.05	28.91	4.99
1365.408	0.018	13.04	0.04	48.75	5.57

Zaldarriaga M., Hui L., Tegmark M., 2001, *ApJ*, **557**, 519
 Zhang Y., Anninos P., Norman M. L., 1995, *ApJ*, **453**, L57

APPENDIX

We formed a line catalog by fitting the observed spectra using VIPER. Table 2 shows few fitted parameters from the VIPER line catalog for spectra towards QSO 1ES1553+113. The first, second, third, fourth, fifth and sixth column shows fitted wavelength (λ in Å), error in wavelength ($d\lambda$ in Å), log of column density ($\log N_{\text{HI}}$ in cm^{-2}), error in log of column density ($d\log N_{\text{HI}}$ in cm^{-2}), b parameter (in km s^{-1}) and error in b parameter (db in km s^{-1}) respectively. The full VIPER line catalog is available online in ASCII format with this paper.

This paper has been typeset from a $\text{\TeX}/\text{\LaTeX}$ file prepared by the author.